Toward single particle reconstruction without particle picking: Breaking the detection limit

Tamir Bendory[a], **Nicolas Boumal**[b], **William Leeb**[c], **Eitan Levin**[a,b], **and Amit Singer**[a,b]

[a]The Program in Applied and Computational Mathematics, Princeton University, Princeton, NJ, USA; [b]Department of Mathematics, Princeton University, Princeton, NJ, USA; [c]School of Mathematics, University of Minnesota, Minneapolis, MN, USA

Cryo–electron microscopy (cryo–EM) is used in structural biology to determine the 3-D structure of molecules. In a cryo-EM experiment, the microscope produces images called micrographs. Projections of the molecule of interest are embedded in the micrographs at unknown locations, and under unknown viewing directions. Standard imaging techniques first locate these projections (detection), then reconstruct the 3-D structure from them. Unfortunately, high noise levels hinder detection. When reliable detection is rendered impossible, the standard techniques fail. This is a problem especially for small molecules, which can be particularly hard to detect. In this paper, we propose a radically different approach: we contend that the structure could, in principle, be reconstructed directly from the micrographs, without intermediate detection and independently of the noise level (provided sufficiently many micrographs are acquired). As a result, even small molecules should be within reach for cryo-EM. To support this claim, we setup a simplified mathematical model and demonstrate how our autocorrelation-based techniques allow to go directly from the micrographs to the sought signals. This involves only one pass over the micrographs, which is desirable for large experiments. Furthermore, concerns regarding experimental bias are reduced as we do not require particle picking via pattern matching. We detail elementary theory for a 1-D version of the simplified model and show how to extend it to 2-D and to single particle reconstruction from synthetic cryo-EM data. We show numerical results, then discuss challenges that lay ahead to turn this proof-of-concept into a competitive alternative to state-of-the-art algorithms.

Cryo-EM | autocorrelation analysis | detection limit

Cryo–electron microscopy (cryo–EM) is an imaging technique in structural biology used for single particle reconstruction (SPR) of macromolecules. In a cryo–EM experiment, biological samples are rapidly frozen in a thin layer of vitreous ice. The microscope produces a 2-D tomographic image of the samples embedded in the ice, called a *micrograph*. Each micrograph contains tomographic projections of the samples at unknown locations and under unknown viewing directions. The goal is to construct 3-D models of the molecular structure from the micrographs.

The signal to noise ratio (SNR) of the projections in the micrographs is a function of two dominating factors. On the one hand, the SNR is a function of the electron dose. To keep radiation damage within acceptable bounds, the dose must be kept low, which leads to high noise levels. On the other hand, the SNR is a function of the molecule size. The smaller the molecules, the fewer detected electrons carry information about them.

All contemporary methods in the field split the reconstruction procedure into two main stages. The first stage consists in extracting the various particle projections from the micrographs. This stage is called *particle picking*. The second stage aims to construct a 3-D model of the molecular structure from these projections. The quality of the reconstruction eventually hinges on the quality of the particle picking stage. Figure 1 illustrates how particle picking becomes increasingly challenging as the SNR degrades.

Crucially, it can be shown that reliable detection of individual particles is impossible below a certain critical SNR. This fact has been recognized early on by the cryo-EM community. In particular, in an influential paper from 1995, Richard Henderson (1) investigates the following questions:

> *For the purposes of this review, I would like to ask the question: what is the smallest size of free-standing molecule whose structure can in principle be determined by phase-contrast electron microscopy? Given what has already been demonstrated in published work, this reduces to the question: what is the smallest size of molecule for which it is possible to determine from images of unstained molecules the five parameters needed to define accurately its orientation (three parameters) and position (two parameters) so that averaging can be performed?*

In that paper and in others that followed (e.g., (2)), it was established that particle picking is impossible for molecules below a certain weight (below ∼50 kDa). Joachim Frank voices a similar observation in his 2017 Nobel prize lecture: "*Using the ribosome as an example, it became clear from the formula we obtained that the single-particle approach to structure research was indeed feasible for molecules of sufficient size: Particle Size > 3/[Contrast^2 × Resolution (as length) × Critical Electron Dose]*" (3). As these two leaders of the cryo-EM community point out, it is impossible to reconstruct small molecules by

---

Significance Statement

It is commonly believed that cryo-EM cannot be used to image the 3-D structure of small molecules (below ∼50kDa). The classical argument is that, due to high noise levels in cryo-EM, small particles cannot be detected reliably in micrographs. Challenging that belief, we demonstrate on a mathematical toy model that detection is not a prerequisite for structure reconstruction. Our reconstruction method is based on autocorrelation analysis. It requires only one pass over the data, so that it should, in principle, be appropriate for high-throughput experiments. This autocorrelation approach could also apply to other applications where the goal is estimation rather than detection.

(a) $\sigma = 0$ **(b)** $\sigma = 0.5$ **(c)** $\sigma = 3$
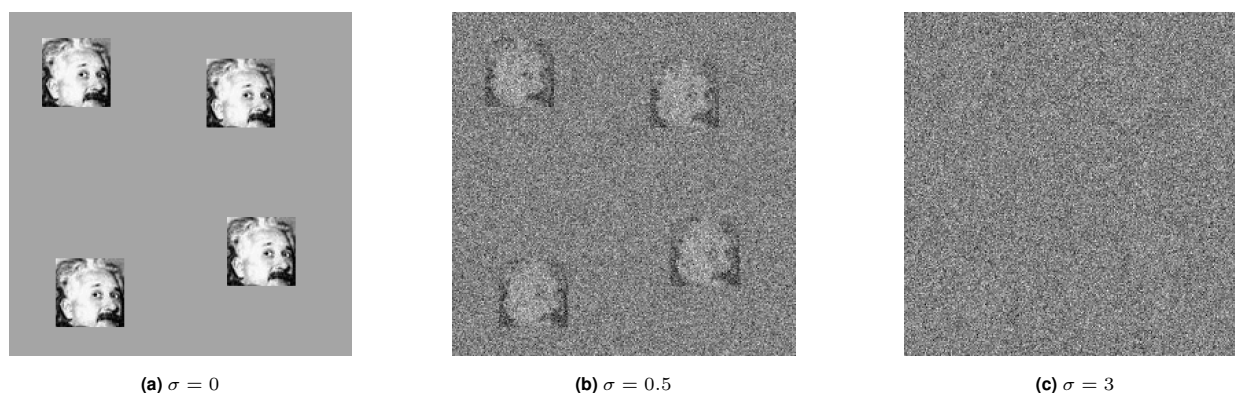
Fig. 1. Example of micrographs of size 250×250 with additive white Gaussian noise of variance σ^2 for increasing values of σ. Each micrograph contains the same four occurrences of a 50×50 image of Einstein. In panel (c), the noise level is such that it is very challenging to locate the occurrences of the planted image. In fact, it can be shown that at low SNR, reliable detection of individual image occurrences is impossible, even if the true image is known. By analogy to cryo-EM, this depicts a scenario where particle picking cannot be done.
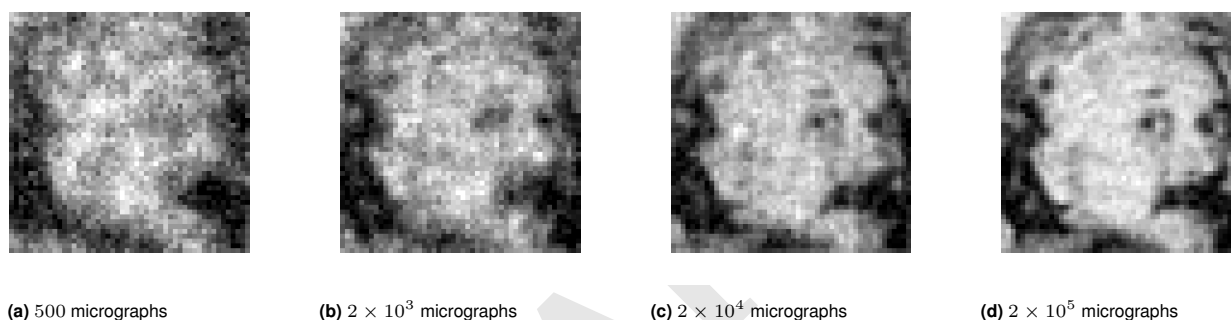

(a) 500 micrographs   **(b)** 2×10^3 micrographs   **(c)** 2×10^4 micrographs   **(d)** 2×10^5 micrographs

Fig. 2. Recovery of Einstein from micrographs at noise level $\sigma = 3$ (see Figure 1(c)). Averaged autocorrelations of the micrographs allow to estimate the power spectrum of the target image. This does not require particle picking. A phase retrieval algorithm (RRR) produces the estimates here shown, initialized randomly. Estimates are obtained from $500, 2 \times 10^3, 2 \times 10^4, 2 \times 10^5$ micrographs (growing across panels), each containing 700 image occurrences on average. [Tamir: I am redoing the exp]

any of the existing computational pipelines for single particle analysis in cryo–EM, because the particles themselves cannot be picked from the micrographs. Yet, imaging such molecules is important for a number of applications (4)

The unique issues raised by small particles have been mitigated by recent technological advances in the field, including the use of Volta phase plates (5, 6) and scaffolding cages (7). Despite this progress, detecting small molecules in the micrographs remains a challenge. We note that nuclear magnetic resonance (NMR) spectroscopy and X-ray crystallography are well suited to reconstruct small molecules. Yet, cryo–EM has a lot to offer even for molecules with already known structures obtained via NMR spectroscopy or X-ray crystallography, because these methods have limited ability to distinguish conformational variability.

In this paper, we argue that there is a gap between the two questions in Henderson's quoted excerpt above, and that one may be able to exploit it to design better reconstruction algorithms. Specifically, the impossibility of particle picking does not necessarily imply impossibility of particle reconstruction. Indeed, the aim is only to reconstruct the molecule: estimating the locations of the particles in the micrograph is merely a helpful intermediate stage when it can be done. Our main message is that the limits particle picking imposes on molecule size do not necessarily translate into limits on particle reconstruction.

As a proof of concept, we first study a toy model for which it is easier to convey the mathematical principles. In this model, an unknown image appears multiple times at unknown locations in each of several micrographs, each affected by additive Gaussian noise—see Figure 1 for an illustration. The goal is to estimate the planted image. The task is challenging in particular when the SNR is low enough that particle picking (identifying the locations of each image in each micrograph) cannot be done reliably. This problem is interesting on its own as it appears in other scientific applications, including spike sorting (8), passive radar (9) and system identification (10).

In order to recover the image, we use autocorrelation analysis. Specifically, we relate the autocorrelations of the micrographs to the autocorrelations of the image. For any noise level, these autocorrelations can be estimated to any desired accuracy, provided that we observe sufficiently many image occurrences and the latter are separated in the micrograph. Importantly, there is no need to detect individual image occurrences. The autocorrelations of the micrographs are straightforward to compute and require only one pass over the data. After estimation of the density of particles in the micrographs, these directly yield estimates for the autocorrelations of the target image itself. To estimate the image itself from its estimated autocorrelations, we solve a nonlinear inverse problem; see for instance Figure 2.

Beyond this 2-D proof of concept, we look toward 3-D reconstruction as well. Zvi Kam (11) first proposed autocorrelation analysis for 3-D reconstruction, under the assumption of perfect particle picking: his method used autocorrelations of the picked, perfectly centered, particles. In contrast, we

derive the mathematical relation between the autocorrelations of the micrographs as a whole and the 3-D volume, under some simplifying conditions. We show a few numerical examples and outline the future developments required to make this method applicable to experimental data.

Another interesting feature of the described approach pertains to model bias, whose importance in cryo-EM was stressed by a number of authors ([12](#)–[15](#)). In the classical "Einstein from noise" experiment, multiple realizations of pure noise are aligned to a picture of Einstein using template matching and then averaged. In ([12](#)), it was shown that the averaged noise rapidly becomes remarkably similar to the Einstein template. In the context of cryo–EM, this experiment exemplifies how prior assumptions about the particles may influence the reconstructed structure. This model bias is common to all particle picking methods based on template matching. In our approach, no templates or human intervention are required, thus significantly reducing concerns about model bias.

1. Proof of concept: A mathematical toy model

In this section, we present a toy model in order to introduce the mathematical principles enabling estimation of a signal in a low SNR regime, even when detection is impossible. Later, we discuss how these principles carry through for the SPR problem. We first formulate the model for 1-D signals to ease exposition.

Let $x \in \mathbb{R}^L$ be the target signal and let $y \in \mathbb{R}^N$ be the observed data, where we assume N is far larger than L. Let $s \in \{0,1\}^{N-L+1}$ be a binary signal indicating (with 1's) the starting positions of all occurrences of x in y, so that, with additive white Gaussian noise:

$$y = x * s + \varepsilon, \qquad \varepsilon \sim \mathcal{N}(0, \sigma^2 I_N), \qquad [1]$$

where $*$ denotes linear convolution. While both x and s are unknown, the goal is only to estimate x from y. This is a key difference with other works on *blind deconvolution*, a longstanding problem arising in a variety of engineering and scientific applications such as astronomy, communication, image deblurring, system identification and optics; see ([16](#)–[19](#)), just to name a few. The parameters of the signal s (the locations of its nonzero values) are the *nuisance variables* of the problem. As will be shown next, in a low SNR environment, estimating s is impossible, whereas estimating x is tractable under some conditions on s.

We assume the binary signal s obeys a *separation condition*:

$$\text{If } s[i] = 1 \text{ and } s[j] = 1 \text{ for } i \neq j, \text{ then } |i-j| \geq 2L-1. \quad [2]$$

In words: the starting positions of any two occurrences must be separated by at least $2L-1$ positions, so that their end points are necessarily separated by at least $L-1$ signal-free entries in the micrograph.

Our problem can be interpreted as a special case of the *system identification* problem. Similarly to Eq. ([1](#)), the forward model takes the form $y = x * w + \varepsilon$, where x is the unknown signal (the system's impulse response), w is an unknown (often random) input sequence, and ε is an additive noise. The goal of this problem is to estimate x, usually referred to as "identifying the system." The question of identifiability of x under this observation model is addressed for certain Gaussian and non-Gaussian w in ([20](#), [21](#)). In the special case where w is binary and satisfies our separation condition, we recover our model.

Likelihood-based methods estimate x as the maximizer of some function $f(x|y)$, where f is derived from the likelihood function of x given the observed signal y. If some prior is assumed on x, then $f(x|y)$ can be taken to be the posterior distribution of x given the data; this is the simplest form of Bayesian inference. Methods based on such formulations are popular nowadays in cryo-EM; see for instance ([22](#), [23](#)). Optimizing the function $f(x|y)$ exactly is often intractable, and thus heuristic methods are used instead. One proposed technique is to use Markov Chain Monte Carlo (MCMC) ([24](#)). In special cases, including the case where w is binary, expectation maximization (EM) has been used ([24](#)). The EM method for discrete w is based on a certain "forward-backward" procedure used in hidden Markov models ([25](#)). However, the complexity of this procedure is superlinear in N, and therefore its usage is limited for big data sets.

Because likelihood methods are computationally expensive, methods based on recovery from moments have also been previously used for system identification. Methods based on the third- and fourth-order moments are described and analyzed in ([26](#)–[28](#)). Building on such ideas, we focus on an autocorrelation analysis for Eq. ([1](#)).

2. The detection limit

In the low SNR regime—even if x is known—estimating the binary sparse signal s is impossible, that is, one cannot reliably detect occurrences of x in the micrograph y. To support this claim, we consider a strictly simpler problem: suppose an oracle identifies for us one interval of length L in the micrograph that either contains a full signal occurrence (plus noise), or contains just noise. Our task is to determine which one it is, that is, to determine whether the corresponding entry of s is 0 or 1. The oracle further provides the signal x, the probability q that the interval contains signal, and the noise variance σ^2.

This decision problem can be abstracted as follows: We have two known vectors $\theta_0 = x$ and $\theta_1 = 0$ in $\mathbb{R}^L$. There is a random variable η taking values 0 or 1 with probabilities q and $1-q$, respectively. We observe a random vector $X \in \mathbb{R}^L$ (an extract of the micrograph) with the following distribution: if $\eta = 0$, then $X \sim \mathcal{N}(\theta_0, \sigma^2 I_L)$ and if $\eta = 1$, then $X \sim \mathcal{N}(\theta_1, \sigma^2 I_L)$.

We observe X, and our task is to estimate η. How reliably can this be done? If $q \geq 1/2$, the constant estimator $\hat{\eta} = 0$ is correct with probability q; likewise, if $q \leq 1/2$, the constant estimator $\hat{\eta} = 1$ is correct with probability $1-q$. The question is, can we do better than this? We prove that, as $\sigma \to \infty$, the answer is no:

Proposition 2.1. *For any deterministic estimator $\hat{\eta}$ of η,*

$$\lim_{\sigma \to \infty} \text{Prob}[\hat{\eta} = \eta] \leq \max(q, 1-q);$$

that is: as the SNR deteriorates, the probability of success is no better than random chance.

The result is proved in Appendix [C](#).

Proposition [2.1](#) implies that in order to estimate the signal at low SNR we must consider methods that aim to estimate the signal x directly, without estimating the nuisance variable s as an intermediate step. In the next sections, we consider autocorrelation analysis for that purpose.

Bendory *et al.*

PNAS | **September 7, 2018** | vol. XXX | no. XX | **3**

3. Autocorrelation analysis

In general, for a signal z of length m, the autocorrelation of order $q = 1, 2, \ldots$ is given for any integer shifts $\ell_1, \ldots, \ell_{q-1}$ by

$$a_z^q[\ell_1, \ldots, \ell_{q-1}] = \frac{1}{m} \sum_{i=-\infty}^{+\infty} z[i] z[i + \ell_1] \cdots z[i + \ell_{q-1}], \quad [3]$$

where indexing of z out of the range $0, \ldots, m-1$ is zero-padded. For our purposes, this will be applied both to x (of length L) and to y (of length N).

Under the separation condition, the relation between autocorrelations of the micrograph and those of x is particularly simple, as we now show. It is useful to introduce some notation: let M denote the number of occurrences of x in y (that is, the number of 1's in s), and let

$$\gamma = \frac{ML}{N} \quad [4]$$

denote the density of x in y (that is, the fraction of entries of y occupied by occurrences of x.) The separation condition imposes $\gamma \leq \frac{L}{2L-1} \approx 1/2$.

For shifts in $0, \ldots, L-1$, the autocorrelation functions of y depend on the corresponding autocorrelations of x, the noise level σ and the support signal s. Importantly, under the separation condition Eq. (2), the dependency on s is only through the density γ. We consider the asymptotic regime where γ remains constant; that is, as N goes to infinity, M also goes to infinity at the same rate (in other words, as we see an increasingly large micrograph, it contains increasingly many signal occurrences, with constant signal density). In that regime, the law of large numbers can be used to show the following statement:

$$\lim_{N \to \infty} a_y^1 \stackrel{a.s.}{=} \gamma a_x^1, \quad [5]$$

where equality holds almost surely (a.s.), meaning it holds with probability one. The randomness is over the Gaussian noise ε; s may be deterministic. Thus, given enough data, if γ is known, we can estimate a_x^1 from y. (We show later how to estimate γ as well.)

We have a similar observation for the second-order autocorrelation: $a_y^2[\ell]$ computes the correlation between y and a copy of y shifted by ℓ entries. Considering ℓ only in the range $0, \ldots, L-1$, one can see that any given occurrence of x in y is only ever correlated with itself, and never with another occurrence. As a result,

$$\lim_{N \to \infty} a_y^2[\ell] \stackrel{a.s.}{=} \gamma a_x^2[\ell] + \sigma^2 \delta[\ell], \quad [6]$$

for $\ell = 0, \ldots, L-1$, where $\delta[\ell]$ equals one for $\ell = 0$ and zero otherwise. The last part captures the autocorrelation of the noise. Notice that, even if σ is unknown, entries $\ell = 1, \ldots, L-1$ still provide useful information about a_x^2.

Along the same lines, one can establish a relation for third-order autocorrelations:

$$\lim_{N \to \infty} a_y^3[\ell_1, \ell_2] \stackrel{a.s.}{=} \gamma a_x^3[\ell_1, \ell_2]$$
$$+ \sigma^2 \gamma a_x^1 \cdot \left(\delta[\ell_1, 0] + \delta[0, \ell_2] + \delta[\ell_1, \ell_2] \right), \quad [7]$$

for $\ell_1, \ell_2 = 0, \ldots, L-1$, where $\delta[\ell_1, \ell_2] := \delta[\ell_1 - \ell_2]$. Here too, few entries are affected by σ in the limit. See Appendix B.

Computing the autocorrelations of the micrograph is straightforward. The natural question, treated next, is whether one can recover x from them.

4. Recovering a signal from autocorrelations

A one-dimensional signal is determined uniquely by its second- and third-order autocorrelations. Indeed, assuming $z[0]$ and $z[L-1]$ are nonzero (otherwise, redefine the length of the signal), we can recover z explicitly using this identity for $k = 0, \ldots, L-1$:

$$z[k] = \frac{z[0]z[k]z[L-1]}{z[0]z[L-1]} = \frac{a_z^3[k, L-1]}{a_z^2[L-1]}. \quad [8]$$

This proves the following useful fact:

Proposition 4.1. *A signal $z \in \mathbb{R}^L$ is determined uniquely from a_z^2 and a_z^3.*

A couple of remarks are in order. First, Eq. (8) is not numerically stable: if $z[0]$ or $z[L-1]$ are close to 0, recovery of z is sensitive to errors in the autocorrelations. In practice, we recover z by fitting it to its autocorrelations using a nonconvex least-squares (LS) procedure, which is empirically more robust to additive noise; we have observed similar phenomena for related problems (29–31). Second, note that the second-order autocorrelation is not by itself sufficient to determine the signal uniquely. However, for dimensions greater than one, almost all signals are determined uniquely up to sign (or phase for complex signals) and reflection through the origin (with conjugation in the complex case) (32). The sign ambiguity can be resolved by the mean of the signal if it is not zero. However, determining the reflection symmetry still requires additional information, beyond the second-order autocorrelation.

The observed moments a_y^1, a_y^2 and a_y^3 of y do not immediately yield the moments of the signal x, as seen by Eq. (5), Eq. (6) and Eq. (7); rather, the two are related by the noise level σ and the ratio γ. We will show, however, that x is still determined by the observed moments of y.

First, we observe that if the noise level σ is known, generally, one can estimate γ from the first two moments of the micrograph. The proof is provided in Appendix D.

Proposition 4.2. *Let $\sigma > 0$ be fixed and assume that the separation condition Eq. (2) holds. If the mean of x is nonzero, then*

$$\gamma \stackrel{a.s.}{=} \lim_{N \to \infty} \frac{L(a_y^1)^2}{a_y^2[0] + 2\sum_{\ell=1}^{L-1} a_y^2[\ell] - \sigma^2}.$$

Using third-order autocorrelation information of y, both the ratio γ and the noise σ are determined. For the following results, when we say that a result holds for a "generic" signal x, we mean that the set of signals which cannot be determined by these measurements has Lebesgue measure zero. In particular, this means that we can recover almost all signals with the given measurements. The proof is provided in Appendix E.

Proposition 4.3. *Assume $L \geq 3$ and assume that the separation condition Eq. (2) holds. In the limit of $N \to \infty$, the observed autocorrelations a_y^1, a_y^2 and a_y^3 determine the ratio γ and noise level σ uniquely for a generic signal x. If $\gamma > \frac{1}{4}$, then this holds for any signal x with nonzero mean.*

From Propositions 4.1 and 4.3 we deduce the following:

Corollary 4.4. *In the limit of $N \to \infty$ and under the separation condition Eq. (2), the signal x, the ratio γ, and the noise level σ are determined from the first three autocorrelation functions of y if either the signal x is generic or x has nonzero mean and $\gamma > \frac{1}{4}$.*

As a side note, under the separation condition, the length L of the signal can also be determined from the autocorrelations in the asymptotic regime, by inspection of the support of a_y^2.

5. Numerical experiments

The technique we advocate allows recovery of a signal hidden in noisy micrographs without detecting the location of the signals embedded in these micrographs. To illustrate the underlying principles of the method, we present several numerical examples for the toy model Eq. (1) and a simple proof of concept for simulated cryo-EM data. Appendix A provides additional details on the experiments. The code to generate all figures is publicly available in https://github.com/PrincetonUniversity/BreakingDetectionLimit.

A. Toy model. In the first experiment, we estimated an 50-by-50 pixel image of Einstein with mean zero from a growing number of micrographs, each of size 4096×4096 pixels. Each micrograph contains, on average, 700 occurrences of the target image at random locations. Thus, about 10% of each micrograph contains signal. The micrographs are contaminated with additive white Gaussian noise with standard deviation $\sigma = 3$, corresponding to SNR $= \frac{M\|x\|_F^2}{\sigma^2 N} \approx 1/370$. This high noise level is illustrated in Figure 1. To simplify the experiment, we assume the number of signal occurrences and the noise standard deviation are known. Micrographs are generated such that any two occurrences are always separated by at least 49 pixels in each direction in accordance with the separation condition Eq. (2).

We compute the average second-order autocorrelation of the micrographs. This is a particularly simple computation which can be efficiently executed with a fast Fourier transform (FFT) in parallel. Given the noise level and number of image repetitions, the second-order autocorrelation of the image can be easily deduced from Eq. (6). Then, to estimate the target image, we resort to a standard phase retrieval algorithm called relaxed-reflect-reflect (RRR) (33), initialized randomly. Relative error is measured as the ratio of the root mean square error to the norm of the ground truth (square root of the sum of squared pixel intensities).

Figure 2 shows several estimated images for a growing number of micrographs, and a movie is available as supplementary material. Figure 5 (see appendix) presents the normalized recovery error as a function of the amount of data available. This is computed after fixing the reflection symmetries (see Section 3). As evidenced by these figures, the ground truth image can be estimated increasingly well from increasingly many micrographs, without particle picking.

In practice, we do not expect to know γ and maybe not even σ. Figure 6 shows recovery of a 1-D signal from the first three autocorrelations of the data. The autocorrelations are computed from noisy micrographs with $\sigma = 3$ that obey the separation condition of Eq. (2). Both the signal and γ are estimated simultaneously from the observed autocorrelations by LS fitting; more details are given in Appendix A. Crucially, the LS does not require knowledge of σ.

B. Cryo-EM. The application of autocorrelation analysis to cryo-EM follows the same mathematical principles. The derivation of the first three autocorrelations of the micrographs and their relations to the volume itself are provided in Appendix F.

In particular, numerical evidence suggests that the third-order autocorrelation uniquely determines the 3-D volume. Figure 3 shows recovery of the 3-D volume from the clean autocorrelations. The details of the reconstruction algorithm are given in Appendix A. Unfortunately, the mapping between the autocorrelations and volume seems to be ill-conditioned, preventing recovery from noisy data. In the next section, we outline how we suggest to overcome the ill-conditioning in future work.

While we cannot provide a 3-D reconstruction from noisy data with the current algorithm, our method can be easily applied to the problem of deciding whether a micrograph contains projections or merely pure noise—a problem considered in classical works in statistics (e.g., (34)) and debates in the cryo-EM community (14). This task can be performed by considering solely the recovered γ (the fraction of pixels occupied by projections in the micrograph), estimated as part of the recovery algorithm. Figure 4 (see appendix) presents excerpts of two noisy micrographs, only one of which contains projections. In the presence of projections, the estimated γ was 0.12, corresponding to approximately 6784 projections. On the other hand, the estimated γ drops to 10^{-5} for the pure noise micrograph, corresponding to less than one projection.

(a) TPRV1 with cutoff $L = 5$
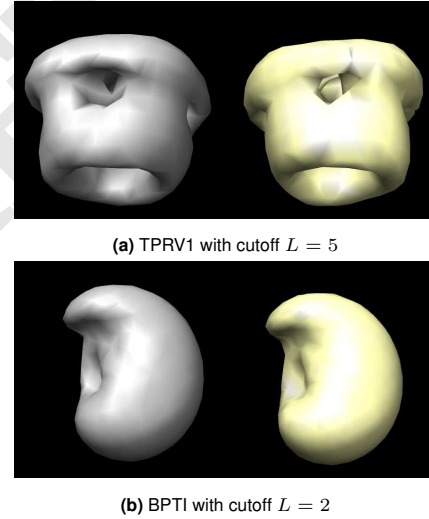

(b) BPTI with cutoff $L = 2$

Fig. 3. Reconstructions from the first, second and third order autocorrelations. The ground truth volumes were expanded according to Eq. (22) with cutoff L. The reconstruction is shown in gray while the (smoothed) ground truth in yellow. [Amit: I suggest calling the spherical harmonics cutoff l_{max} rather than L. Previously, L is used for the size of the signal or for the size of images LxL. So, it is quite confusing to use L in a completely different context. You would need to make changes in many other places as well (e.g., eq.(23) and the labels (a) and (b) in this figure, are just two examples), in order to avoid this notation overload.]

6. Discussion

In the simplified mathematical model we examined, we showed it is possible to estimate a signal without detecting its appearances. Our strategy is to compute autocorrelation functions of the micrographs and to relate these statistics to the unknown signal's parameters. Recovering the parameters from the statistics reduces to solving a set of polynomial equations.

We also showed how this technique can, in principle, be applied to cryo-EM. Crucially, the outlined approach involves no particle picking, hence a fortiori no viewing direction estimation. Concerns for model bias are also greatly reduced since no template matching is involved. Additionally, our
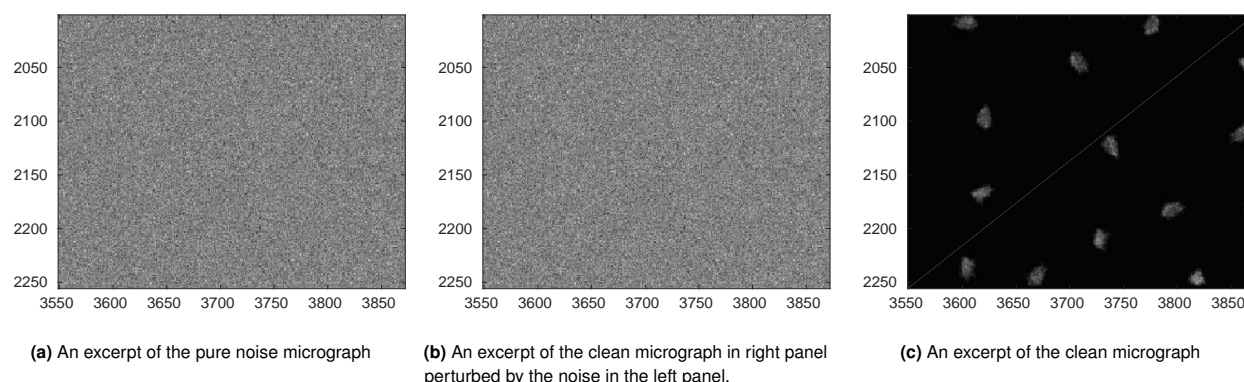
(a) An excerpt of the pure noise micrograph

(b) An excerpt of the clean micrograph in right panel perturbed by the noise in the left panel.

(c) An excerpt of the clean micrograph

Fig. 4. All micrographs are of size 7420^2 pixels and the projections are taken from a volume of size 31^3. The added noise was drawn from i.i.d. Gaussian distribution with zero mean and standard deviation 25, corresponding to an SNR below $1/1024$. The noise realization is identical in both micrographs. [Diagonal line] [Amit: need to specify which molecule is projected to create micrographs shown in (b) and (c). This is not mentioned in the text either.]

technique also allows the use of much lower defocus values. Lower defocus means lower contrast, but will maintain higher frequency information. Consequently, we may be able to get high resolution reconstructions from fewer micrographs.

Looking towards applying the framework to encompass all important features of real cryo-EM experiments, our work implies that it might be possible to reconstruct small molecules, particularly, molecules that are too small to be detected in micrographs. In pursuing this research direction, our goal is to significantly increase the range of molecules to which cryo-EM can be successfully applied. We recognize that significant challenges lay ahead for the implementation of the proposed approach to 3-D reconstruction directly from the micrographs. We discuss a few now.

The numerical experiments we have performed reveal that the third-order autocorrelation may not be enough for 3-D reconstruction in practice, due to high sensitivity. This suggests that fourth-order autocorrelation may be necessary. This in turn would imply that the procedure might require a large amount of data.[*] Recent trends in high-throughput cryo-EM technology give hope that this may be a lesser concern in the long term. Still, large amounts of data also require large amounts of computation. On this front, we note that computing autocorrelations can be executed efficiently on CPUs and GPUs, and in parallel across micrographs. It can even be done in streaming mode, as only one pass through each micrograph is necessary. The output of this data processing stage is a summary in the form of autocorrelation estimates: its size is a function of the resolution, not a function of the number of observed micrographs. Subsequent steps, which involve solving the system of polynomial equations, scale only in the size of that summary. Of course, an important question then is whether the equations can be solved accurately and efficiently in practice.

Beyond data acquisition and computational challenges, there are modeling issues to consider. In contrast to the simplifying assumptions we have made above, the noise might be colored; the viewing directions of the particles may be distributed non-uniformly; their may be conformational heterogeneity; particles generally do not satisfy our separation condition; and micrographs undergo a contrast transfer func-

tion which we have omitted. All of these aspects can be handled with the same general strategy: establish a forward model relating the expected autocorrelations of the micrographs to the target volume(s) and all parameters necessary to model the above effects. For instance, for colored noise, the forward model may involve multiple parameters to capture the power spectrum of the noise instead of the single parameter σ^2. The separation condition could be relaxed by assuming a Poisson process of particle distribution in the micrograph, in which case the forward model will involve the Poisson parameter. All these aspects must be taken into account so the method can be applied on experimental data. We hope to take care of these issues in future research.

1. Henderson R (1995) The potential and limitations of neutrons, electrons and X-rays for atomic resolution microscopy of unstained biological molecules. *Quarterly reviews of biophysics* 28(2):171–193.
2. Glaeser RM (1999) Electron crystallography: present excitement, a nod to the past, anticipating the future. *Journal of structural biology* 128(1):3–14.
3. Frank J (2018) Single-particle reconstruction of biological molecules-story in a sample (Nobel lecture). *Angewandte Chemie International Edition.*
4. Scapin G, Potter CS, Carragher B (2018) Cryo-EM for small molecules discovery, design, understanding, and application. *Cell Chemical Biology.*
5. Khoshouei M, Radjainia M, Baumeister W, Danev R (2017) Cryo-EM structure of haemoglobin at 3.2 å determined with the Volta phase plate. *Nature communications* 8:16099.
6. Liang YL et al. (2017) Phase-plate cryo-EM structure of a class B GPCR–G-protein complex. *Nature* 546(7656):118.
7. Liu Y, Gonen S, Gonen T, Yeates TO (2018) Near-atomic cryo-EM imaging of a small protein displayed on a designed scaffolding system. *Proceedings of the National Academy of Sciences* 115(13):3362–3367.
8. Lewicki MS (1998) A review of methods for spike sorting: the detection and classification of neural action potentials. *Network: Computation in Neural Systems* 9(4):R53–R78.
9. Gogineni S, Setlur P, Rangaswamy M, Nadakuditi RR (2018) Passive radar detection with noisy reference channel using principal subspace similarity. *IEEE Transactions on Aerospace and Electronic Systems* 54(1):18–36.
10. Ljung L (1998) System identification in *Signal analysis and prediction*. (Springer), pp. 163–173.
11. Kam Z (1980) The reconstruction of structure from electron micrographs of randomly oriented particles. *Journal of Theoretical Biology* 82(1):15–39.
12. Shatsky M, Hall RJ, Brenner SE, Glaeser RM (2009) A method for the alignment of heterogeneous macromolecules from electron microscopy. *Journal of structural biology* 166(1):67–78.
13. van Heel M, Schatz M, Orlova E (1992) Correlation functions revisited. *Ultramicroscopy* 46(1–4):307–316.
14. Henderson R (2013) Avoiding the pitfalls of single particle cryo-electron microscopy: Einstein from noise. *Proceedings of the National Academy of Sciences* 110(45):18037–18041.
15. van Heel M (2013) Finding trimeric HIV-1 envelope glycoproteins in random noise. *Proceedings of the National Academy of Sciences* 110(45):E4175–E4177.
16. Jefferies SM, Christou JC (1993) Restoration of astronomical images by iterative blind deconvolution. *The Astrophysical Journal* 415:862.
17. Shalvi O, Weinstein E (1990) New criteria for blind deconvolution of nonminimum phase systems (channels). *IEEE Transactions on information theory* 36(2):312–321.
18. Ayers G, Dainty JC (1988) Iterative blind deconvolution method and its applications. *Optics letters* 13(7):547–549.

---

[*]Whether or not this large amount of data would be necessary for any method to succeed given the unfavorable SNR remains an open question.

19. Abed-Meraim K, Qiu W, Hua Y (1997) Blind system identification. *Proceedings of the IEEE* 85(8):1310–1322.

20. Benveniste A, Goursat M, Ruget G (1980) Robust identification of a nonminimum phase system: Blind adjustment of a linear equalizer in data communications. *IEEE Transactions on Automatic Control* 25(3):385–399.

21. Kormylo J, Mendel J (1983) Identifiability of nonminimum phase linear stochastic systems. *IEEE transactions on automatic control* 28(12):1081–1090.

22. Sigworth F (1998) A maximum-likelihood approach to single-particle image refinement. *Journal of structural biology* 122(3):328–339.

23. Scheres SH (2012) RELION: implementation of a bayesian approach to cryo-em structure determination. *Journal of structural biology* 180(3):519–530.

24. Cappé O, Doucet A, Lavielle M, Moulines E (1999) Simulation-based methods for blind maximum-likelihood filter identification. *Signal processing* 73(1-2):3–25.

25. Rabiner LR (1989) A tutorial on hidden Markov models and selected applications in speech recognition. *Proceedings of the IEEE* 77(2):257–286.

26. Lii K, Rosenblatt M, et al. (1982) Deconvolution and estimation of transfer function phase and coefficients for nongaussian linear processes. *The annals of statistics* 10(4):1195–1208.

27. Giannakis GB, Mendel JM (1989) Identification of nonminimum phase systems using higher order statistics. *IEEE Transactions on Acoustics, Speech, and Signal Processing* 37(3):360–377.

28. Tugnait J (1984) *Identification of nonminimum phase linear stochastic systems.* No. 23, pp. 342–347.

29. Bendory T, Boumal N, Ma C, Zhao Z, Singer A (2017) Bispectrum inversion with application to multireference alignment. *IEEE Transactions on Signal Processing* 66(4):1037–1050.

30. Boumal N, Bendory T, Lederman RR, Singer A (2018) *Heterogeneous multireference alignment: A single pass approach.* (IEEE), pp. 1–6.

31. Abbe E et al. (2017) Multireference alignment is easier with an aperiodic translation distribution. *arXiv preprint arXiv:1710.02793.*

32. Hayes M (1982) The reconstruction of a multidimensional sequence from the phase or magnitude of its fourier transform. *IEEE Transactions on Acoustics, Speech, and Signal Processing* 30(2):140–154.

33. Elser V (2017) Matrix product constraints by projection methods. *Journal of Global Optimization* 68(2):329–355.

34. Donoho D, Jin J, et al. (2004) Higher criticism for detecting sparse heterogeneous mixtures. *The Annals of Statistics* 32(3):962–994.

35. Bandeira AS, Blum-Smith B, Perry A, Weed J, Wein AS (2017) Estimation under group actions: recovering orbits from invariants. *arXiv preprint arXiv:1712.10163.*

36. Zhang Y, Kuo HW, Wright J (2018) Structured local optima in sparse blind deconvolution. *arXiv preprint arXiv:1806.00338.*

37. Boumal N, Mishra B, Absil PA, Sepulchre R (2014) Manopt, a Matlab toolbox for optimization on manifolds. *Journal of Machine Learning Research* 15:1455–1459.

38. Pettersen EF et al. (2004) UCSF chimera—a visualization system for exploratory research and analysis. *Journal of computational chemistry* 25(13):1605–1612.

39. Stewart GW (1980) The efficient generation of random orthogonal matrices with an application to condition estimators. *SIAM Journal on Numerical Analysis* 17(3):403–409.

40. Bhamre T, Zhang T, Singer A (2017) Anisotropic twicing for single particle reconstruction using autocorrelation analysis. *arXiv preprint arXiv:1704.07969.*

41. Levin E, Bendory T, Boumal N, Kileel J, Singer A (2017) 3D ab initio modeling in cryo-EM by autocorrelation analysis. *arXiv preprint arXiv:1710.08076.*

42. Natterer F (1986) *The mathematics of computerized tomography.* (SIAM) Vol. 32.

43. Slepian D (1964) Prolate spheroidal wave functions, Fourier analysis and uncertainty—iv: Extensions to many dimensions; generalized prolate spheroidal functions. *The Bell System Technical Journal* 43(6):3009–3057.

44. Landa B, Shkolnisky Y (2017) Steerable principal components for space-frequency localized images. *SIAM journal on imaging sciences* 10(2):508–534.

45. Zhao Z, Shkolnisky Y, Singer A (2016) Fast steerable principal component analysis. *IEEE transactions on computational imaging* 2(1):1–12.
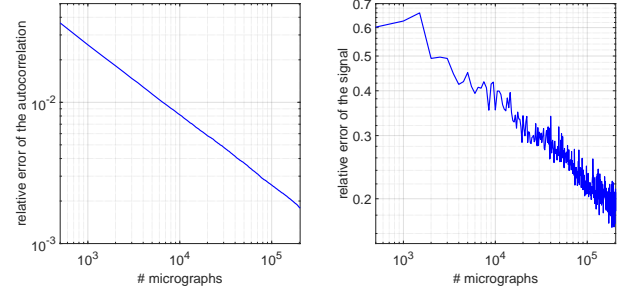
Acknowledgment

A. Numerical experiments details

We run the toy model experiments on a shared computer with 144 logical CPUs of type Intel(R) Xeon(R) CPU E7-8880 v3

Fig. 5. Relative error curves for the experiment of Figure 2.

@ 2.30GHz and 792 Gb of RAM; we use at most 72 of these CPUs.

2-D experiment. For the 2-D experiment shown in Figures 2 and 5, we generated micrographs of size 4096×4096 pixels. In each micrograph, we placed Einstein's image (of zero mean) of size 50×50 in random locations, while preserving the separation condition Eq. (2). This is done by randomly selecting 4000 placements in the micrograph, one at a time with an accept/reject rule based on the separation condition and locations picked so far. On average, 700 images are placed in each micrograph. Then, i.i.d. Gaussian noise with standard deviation $\sigma = 3$ is added, inducing an SNR of approximately $1/370$. An example of a micrograph's excerpt is presented in the right panel of Figure 1.

In this experiment, we assume to know the noise level σ and the total number of occurrences of the target image across all micrographs. In stark contrast with the 1-D setup, the second-order autocorrelation determines almost any target image uniquely, up to reflection through the origin. This is because the second-order autocorrelations correspond to the Fourier magnitudes of the signal through the 2-D Fourier transform. Therefore, we estimate the signal's Fourier magnitudes (or power spectrum) from the Fourier magnitudes of the micrographs, at the cost of one 2-D fast Fourier transform (FFT) per micrograph. These can be computed highly efficiently and in parallel. Computing the power spectrum of 200 micrographs took less than 23 seconds.

To recover the target image from the estimated power spectrum, we use a standard phase retrieval algorithm called relaxed-reflect-reflect (RRR). This algorithm iterates the map

$$z \leftarrow z + \beta(P_2(2P_1(z) - z) - P_1(z)),$$

on an image z of size $2L \times 2L$. We set the parameter β to 1. The map is designed so that, if the estimated power spectrum is exact, then fixed points contain Einstein's image in the upper-left corner of size $L \times L$, possibly reflected through its origin, and zeros elsewhere. The operator $P_2(z)$ combines the Fourier phases of the current estimation z with the estimated Fourier magnitudes. The operator $P_1(z)$ zeros out all entries of z outside the $L \times L$ upper-left corner. In all experiments, the algorithm halted after a fixed number of 2000 iterations. Running the RRR took about 3 seconds.

The computational complexity scales as $O(N^2 L^2 + F(L))$, where F is the complexity of the RRR algorithm and N^2 stands for the total number of pixels across micrographs.

Bendory *et al.*

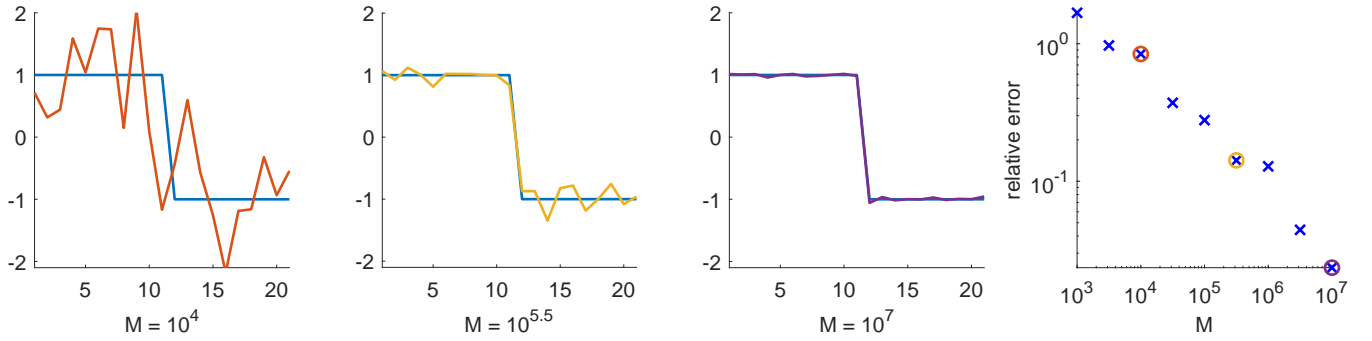PNAS | **September 7, 2018** | vol. XXX | no. XX | **7**

Fig. 6. Recovery of a 1-D signal of length $L = 21$ at noise level $\sigma = 3$ from M repetitions. The length of the micrograph was set to be $N = 410 * M$. The first three panels (left to right) show reconstruction with different M values compared to the ground truth signal (in blue). The true value of γ is 0.0512. The relative errors of γ for the three panels are: $4.8\%, 4\%, 1.2\%$. The right panel shows the relative error as a function of M.

1-D experiment. For the 1-D experiment depicted in Figure 6, we used a signal of length $L = 21$ and generated an observation y of length $N = 10(2L − 1)M$, where M is the number of repetitions. The observation was generated by randomly selecting placements in y, one at a time with an accept/reject rule based on the separation condition and locations picked so far until reaching the desired number of signal occurrences. Then, i.i.d. Gaussian noise with mean zero and standard deviation $\sigma = 3$ is added, to form the observed y. The resulting SNR of y is about $1/175$.

Given the observation y, we proceed to compute the autocorrelations. We excluded biased elements of the autocorrelations; that is $a_y^2[\ell_1]$ and $a_y^3[\ell_1, \ell_2]$ such that ℓ_1, ℓ_2 or $\ell_1 − \ell_2$ are zero. This has the practical effect that we need not know σ. By also taking symmetries into account, the third-order autocorrelation contains $\frac{(L−1)(L−2)}{2}$ remaining entries. Thus, in total we have

$$1 + (L − 1) + \frac{(L−1)(L−2)}{2} = \frac{1}{2}L(L−1) + 1$$

coefficients. This redundancy suggests that it might be possible to estimate several signals simultaneously (compare with (30, 35)). In practice, the autocorrelations are computed on disjoint segments of y of length $100 \cdot 10^6$ (if the length of the measurement is larger than that) and added up, without correction for the junction points. Segments are handled sequentially on a GPU, as GPUs are particularly well suited to execute simple instructions across large vectors of data. If multiple GPUs are available, segments can of course be handled in parallel. [Do we use GPUs? Running times]

Having computed the moments of interest, we now estimate the signal x and coefficient γ which agree with the data. We choose to do so by running an optimization algorithm on the following nonlinear LS problem:

$$\min_{\substack{\hat{x} \in \mathbb{R}^W \\ \hat{\gamma} > 0}} w_1 \left(a_y^1 − \hat{\gamma} a_{\hat{x}}^1 \right)^2 + w_2 \sum_{\ell=1}^{L−1} \left(a_y^2[\ell] − \hat{\gamma} a_{\hat{x}}^2[\ell] \right)^2$$
$$+ w_3 \sum_{\substack{2 \le \ell_1 \le L−1 \\ 1 \le \ell_2 \le \ell_1 − 1}} \left(a_y^3[\ell_1, \ell_2] − \hat{\gamma} a_{\hat{x}}^3[\ell_1, \ell_2] \right)^2, \quad [9]$$

where $W \ge L$ is the length of the sought signal and the weights are set to $w_1 = 1/2, w_2 = 1/2n_2, w_3 = 1/2n_3$, where n_2, n_3 are the number of moments used: $n_2 = L − 1$, $n_3 = \frac{(L−1)(L−2)}{2}$ (weights could also be set in accordance with variance estimates as in (30)).

Setting $W = L$ (as is a priori desired) is problematic because the above optimization problems appears to have numerous poor local optimizers. A similar phenomenon was recently observed in a related problem (36). Thus, we first run the optimization with $W = 2L − 1$. This problem appears to have few poor local optima, perhaps because the additional degrees of freedom allow for more escape directions. Since we hope the signals estimated this way correspond to the true signals zero-padded to length W, we extract from each one a subsignal of length L that has largest ℓ_2-norm. This estimator is then used as initial iterate for Eq. (9), this time with $W = L$. We find that this procedure is reliable for a wide range of experimental parameters. To solve Eq. (9), we run the trust-region method implemented in Manopt (37), which allows to treat the positivity constraints on coefficients $\hat{\gamma}$. Notice that the cost function is a polynomial in the variables, so that it is straightforward to compute it and its derivatives.

The computational complexity scales as $O(NL^2 + F(L))$, where F is the complexity of the solving the LS.

3-D experiments. [We need to add description of computer + running times] For the experiments in Figure 4, we computed the analytical first three autocorrelations of the volume as explained in Appendix F. To estimate the coefficients of the volume itself, we solve the LS problem

$$\min_{\hat{x}, \hat{\gamma}} w_1 |\mathfrak{a}_x^1 − \hat{\gamma}\mathfrak{a}_{\hat{x}}^1|^2 + w_2 \|\mathfrak{a}_x^2 − \hat{\gamma}\mathfrak{a}_{\hat{x}}^2\|_2^2 + w_3 \|\mathfrak{a}_x^3 − \hat{\gamma}\mathfrak{a}_{\hat{x}}^3\|_F^2, \quad [10]$$

where the explicit expressions of $\mathfrak{a}_x^1$, $\mathfrak{a}_x^2$ and $\mathfrak{a}_x^3$ are given in Eq. (43), Eq. (42) and Eq. (41), respectively. In the experiments, we set $w_1 = w_2 = w_3 = 1$. The LS problem was solved using Matlab's `lsqnonlin` solver for nonlinear LS problems. The expected $\hat{\gamma}$ in this experiment is one.

The computational complexity scales as $O(N^2L^6 + F(L))$, where F is the complexity of the solving the LS and N^2 is the total number of pixels across micrographs. The factor of L^6 comes from [to continue]

The true volume used in the experiments in Figures 4 and 3b was the Bovine Pancreatic Trypsin Inhibitor (BPTI) mutant with altered binding loop sequence, whos atomic model is available in the Protein Data Bank (PDB) as 1QLQ†. We generated an EM map from this atomic model in UCSF Chimera (38) at a resolution of 5 Å, and cropped it to remove zeros at the boundary to obtain a volume of size 31^3. For the experiment in Figure 3b, the volume was downsampled to size 20^3. For the

---

† https://www.rcsb.org

Bendory *et al.*

experiment in Figure 3a, we used the TRPV1 in complex with DkTx and RTX, whose EM map is available in the Electron Microscopy Data Bank (EMDB) as EMD-8117[‡]. The original map has size 192^3, and was downsampled to size 20^3. To generate the ground truth for our reconstructions, we expanded both volumes as in Eq. (22) with cutoff $L = 5$ for TRPV1 and $L = 2$ for BPTI. For the TRPV1 reconstruction, the optimizer converged to a point giving relative ℓ_2 error of 10^{-6} in the first three autocorrelations and an error of 10^{-1} in the expansion coefficients of the volume. For the BPTI reconstruction, the errors in the autocorrelations were 10^{-6}, 10^{-7} and 10^{-8} for the third, second and first autocorrelations, respectively, while the error in the expansion coefficients of the volume was 5×10^{-2}. This illustrates the ill-conditioning of the map between the volume and its first three autocorrelations that prevents us from obtaining results from noisy data.

The micrographs for the experiment presented in Figure 4 were generated as follows. We sample rotation matrices from $SO(3)$ uniformly at random using the QR-based algorithm described in (39), and generate the projection of the volume corresponding to that rotation matrix using `cryo_project` in ASPIRE[§]. We keep track of the indices at which the upper left corner of a projection can be placed without violating the separation condition, so all projections are separated by at least 30 pixels in each dimension. We continue adding projections to the micrograph until no more projections can be added without violating the separation condition. [Nico: is this really how the procedure works? Or is it just that after a few failed attempts, we abandon? Also, the text doesn't say if the projections are placed at random, but I'm assuming they are ?] Then, the LS problem Eq. (10) was solved assuming the spherical harmonic cutoff for the volume is $L = 0$, which is sufficient to recover a significant $\widehat{\gamma}$ in the presence of projections in the micrograph.

B. Derivation of the identities in Section 3

We consider the asymptotic regime $N, M \to \infty$ and assume that $M = \Omega(N)$, so that

$$\gamma := \frac{ML}{N} > 0.$$

Any vectors with indices out of range are given value 0.

We start by considering the mean of the data:

$$a_y^1 = \frac{1}{N} \sum_{i=0}^{N-1} y[i] = \frac{1}{N/L} \sum_{j=0}^{M-1} \frac{1}{L} \sum_{i=0}^{L-1} x[i] + \underbrace{\frac{1}{N} \sum_{i=0}^{N-1} \varepsilon[i]}_{\text{noise term}} \xrightarrow{a.s.} \gamma a_x^1,$$

where the noise term converges to zero almost surely (a.s.) by the strong law of large numbers.

We proceed with the (second-order) autocorrelation for fixed $\ell \in [0, \ldots, L-1]$. We can compute:

$$a_y^2[\ell] = \frac{1}{N} \sum_{i=0}^{N-1-\ell} y[i]y[i+\ell]$$

$$= \underbrace{\frac{1}{N} \sum_{j=1}^{M} \sum_{i=0}^{L-\ell-1} x[i]x[i+\ell]}_{\text{signal term}} + \underbrace{\frac{1}{N} \sum_{i=0}^{N-1-\ell} \varepsilon[i]\varepsilon[i+\ell]}_{\text{noise term}}$$

$$+ \underbrace{\frac{1}{N} \sum_{j=1}^{M} \sum_{i=0}^{L-1} x[i](\varepsilon[s_j + i + \ell] + \varepsilon[s_j + i - \ell])}_{\text{cross-term}}.$$

The cross-term is linear in the noise, and is easily shown to vanish almost surely in the limit $N \to \infty$, by the strong law of large numbers. We break the signal term into M different sums, each containing one copy of the signal. This gives:

$$\frac{1}{N} \sum_{j=1}^{M} \sum_{i=0}^{L-\ell-1} x[i]x[i+\ell] = \frac{ML}{N} \frac{1}{L} \sum_{i=0}^{L-\ell-1} x[i]x[i+\ell]$$

$$\xrightarrow{N \to \infty} \gamma a_x^2[\ell]. \qquad [11]$$

We next analyze the pure noise term. When $\ell \neq 0$, we can break the noise term into a sum of independent terms:

$$\frac{1}{N} \sum_{i=0}^{N-1-\ell} \varepsilon[i]\varepsilon[i+\ell] = \frac{1}{\ell} \sum_{i=0}^{\ell-1} \frac{1}{N/\ell} \sum_{j=0}^{N/\ell-2} \varepsilon[j\ell + i]\varepsilon[(j+1)\ell + i].$$

Each sum $\frac{1}{N/\ell} \sum_{j=0}^{N/\ell-2} \varepsilon[j\ell + i]\varepsilon[(j+1)\ell + i]$ is an average of N/ℓ independent terms with expectation zero, hence converges to zero almost surely as $N \to \infty$. If $\ell = 0$, then we have:

$$\frac{1}{N} \sum_{i=0}^{N-1} \varepsilon^2[i] \xrightarrow{a.s.} \sigma^2.$$

We now analyze the third-order autocorrelation. Let us fix $\ell_1 \geq \ell_2 \geq 0$. We have:

$$a_y^3[\ell_1, \ell_2] = \frac{1}{N} \sum_{i=0}^{N-1-\ell_1} y[i]y[i+\ell_1]y[i+\ell_2]$$

$$= \underbrace{\frac{ML}{N} \frac{1}{M} \sum_{j=1}^{M} \frac{1}{L} \sum_{i=0}^{L-1-\ell_1} x[i]x[i+\ell_1]x[i+\ell_2]}_{(1)}$$

$$+ \underbrace{\frac{1}{N} \sum_{i=0}^{N-1-\ell_1} \varepsilon[i]\varepsilon[i+\ell_1]\varepsilon[i+\ell_2]}_{(2)}$$

$$+ \underbrace{\frac{1}{N} \sum_{j=1}^{M} \sum_{i=0}^{L-1} x[i]\varepsilon[s_j + i + \ell_1]\varepsilon[s_j + i + \ell_2]}_{(3)}$$

$$+ \underbrace{\frac{1}{N} \sum_{j=1}^{M} \sum_{i=0}^{L-1} \varepsilon[s_j + i - \ell_1]x[i]\varepsilon[s_j + i + \ell_2 - \ell_1]}_{(4)}$$

$$+ \underbrace{\frac{1}{N} \sum_{j=1}^{M} \sum_{i=0}^{L-1} \varepsilon[s_j + i - \ell_2]\varepsilon[s_j + i + \ell_1 - \ell_2]x[i]}_{(5)}$$

$$+ \underbrace{\frac{1}{N} \sum_{j=1}^{M} \sum_{i=0}^{L-\ell_1+\ell_2-1} \varepsilon[s_j + i - \ell_2]x[i+\ell_1-\ell_2]x[i]}_{(6)}$$

$$+ \frac{1}{N}\sum_{j=1}^{M}\underbrace{\sum_{i=0}^{L-\ell_2-1} x[i]\varepsilon[s_j+i+\ell_1]x[i+\ell_2]}_{(7)}$$

$$+ \frac{1}{N}\sum_{j=1}^{M}\underbrace{\sum_{i=0}^{L-\ell_1-1} x[i]x[i+\ell_1]\varepsilon[s_j+i+\ell_2]}_{(8)}.$$

Terms (6), (7) and (8) are linear in ε, and can easily be shown to converge to 0 almost surely by the law of large numbers, by similar arguments as used previously. Term (1) converges to $\gamma a_x^3[\ell_1,\ell_2]$ almost surely, for the same reasons as Eq. (11). To deal with terms (2)–(5), we must distinguish between different values of ℓ_1 and ℓ_2.

Case 1: $0 < \ell_2 < \ell_1$. Here, all summands with elements of ε involve products of distinct entries, which have expected value 0. Consequently, the usual argument shows that terms (2)–(5) all converge to 0 almost surely as $N \to \infty$.

Case 2: $0 = \ell_2 < \ell_1$. Term (2) is an average of products of the form $\varepsilon[i]^2\varepsilon[i+\ell_1]$, which have mean zero; consequently, term (2) converges to 0 almost surely. The same argument as for Case 1 shows that (3) and (5) also converge to 0. For term (4), we write:

$$\frac{1}{N}\sum_{j=1}^{M}\sum_{i=0}^{L-1}\varepsilon[s_j+i-\ell_1]x[i]\varepsilon[s_j+i+\ell_2-\ell_1]$$

$$= \frac{ML}{N}\frac{1}{L}\sum_{i=0}^{L-1}x[i]\frac{1}{M}\sum_{j=1}^{M}\varepsilon[s_j+i-\ell_1]^2$$

$$\xrightarrow{a.s.} \gamma\frac{1}{L}\sum_{i=0}^{L-1}x[i]\sigma^2 = \gamma a_x^1\sigma^2.$$

Case 3: $0 < \ell_2 = \ell_1$. An argument nearly identical to that for Case 2 shows that terms (2), (4) and (5) converge to 0, while term (3) converges to $\gamma a_x^1\sigma^2$.

Case 4: $0 = \ell_2 = \ell_1$. The same argument as for term (4) in Case 2 shows that terms (3), (4) and (5) all converge to $\gamma a_x^1\sigma^2$. Term (2) is an average of $\varepsilon[i]^3$, which is mean zero; consequently, it converges to 0.

This completes the proof.

C. Proof of Proposition 2.1

The proof is based on a variant of the Neyman–Pearson Lemma to derive the best (deterministic) estimator $\hat\eta$. Take any estimator $\hat\eta$; it is characterized by S: the set of X's where $\hat\eta = 1$, where X is a random vector as defined above Proposition 2.1. We write Prob_i to mean the probability conditional on the event $\eta = i$; that is, $\mathrm{Prob}_i[A] = \mathrm{Prob}[A|\eta = i]$. Then, the probability that $\hat\eta$ fails is:

$$\mathrm{Prob}[\hat\eta \neq \eta] = q\mathrm{Prob}_0[\hat\eta = 1] + (1-q)\mathrm{Prob}_1[\hat\eta = 0]$$
$$= q\mathrm{Prob}_0[\hat\eta = 1] + (1-q)(1 - \mathrm{Prob}_1[\hat\eta = 1])$$
$$= q\mathrm{Prob}_0[\hat\eta = 1] + (1-q) - (1-q)\mathrm{Prob}_1[\hat\eta = 1]$$
$$= (1-q) + \int_S (qf_0(x) - (1-q)f_1(x))dx, \quad [12]$$

where $f_i(x)$ is the normal density with mean θ_i and variance σ^2. The best estimator of η based on X minimizes the failure

probability; hence, it minimizes the integral in Eq. (12) through an appropriate choice of the set S. This is achieved by picking all x's such that the integrand is nonpositive:

$$S = \{x : qf_0(x) - (1-q)f_1(x) \leq 0\}.$$

With $\Lambda(x) = f_0(x)/f_1(x)$ and $b = (1-q)/q$, the corresponding estimator is:

$$\hat\eta = \begin{cases} 1 \text{ if } \Lambda(x) \leq b, \\ 0 \text{ if } \Lambda(x) > b. \end{cases}$$

Taking logarithms, the set S can be rewritten as the set of x's where:

$$-\|x - \theta_0\|^2 \leq -\|x - \theta_1\|^2 + 2\sigma^2\log(b),$$

or equivalently

$$\langle x, \theta_1 - \theta_0\rangle \geq \frac{\|\theta_1\|^2 - \|\theta_0\|^2}{2} - \sigma^2\log(b).$$

Now let us compute the probability of failure conditional on the event $\eta = 0$. In this case, failure occurs when $X \in S$. Since $X|(\eta = 0) \sim N(\theta_0, \sigma^2)$, we can write $X|(\eta = 0) = \sigma Z + \theta_0$, where $Z \sim N(0, I)$. On that condition,

$$\langle X, \theta_1 - \theta_0\rangle = \sigma\langle Z, \theta_1 - \theta_0\rangle + \langle \theta_0, \theta_1 - \theta_0\rangle$$
$$= \sigma\langle Z, \theta_1 - \theta_0\rangle + \langle\theta_0, \theta_1\rangle - \|\theta_0\|^2,$$

and failure occurs when

$$\sigma\langle Z, \theta_1 - \theta_0\rangle \geq \frac{\|\theta_1\|^2 + \|\theta_0\|^2}{2} - \langle\theta_0, \theta_1\rangle - \sigma^2\log(b)$$
$$= \frac{1}{2}\|\theta_1 - \theta_0\|^2 - \sigma^2\log(b).$$

Define $Y = \langle Z, \theta_1 - \theta_0\rangle \sim N(0, \|\theta_1 - \theta_0\|^2)$ and divide through by σ. The above event is equivalent to:

$$Y \geq \frac{c}{\sigma} - \sigma\log(b),$$

where $c = \|\theta_1 - \theta_0\|^2/2$. For simplicity, let us assume $\|\theta_1 - \theta_0\| = 1$, so that $Y \sim N(0, 1)$. Then,

$$\mathrm{Prob}_0[\hat\eta = 1] = \mathrm{Prob}\left[Y \geq \frac{c}{\sigma} - \sigma\log(b)\right], \quad Y \sim N(0, 1).$$

Similarly,

$$\mathrm{Prob}_1[\hat\eta = 0] = \mathrm{Prob}\left[Y \geq \frac{c}{\sigma} + \sigma\log(b)\right], \quad Y \sim N(0, 1).$$

Thus, the overall probability of failure is:

$$\mathrm{Prob}[\hat\eta \neq \eta] = q\mathrm{Prob}\left[Y \geq \frac{c}{\sigma} - \sigma\log(b)\right]$$
$$+ (1-q)\mathrm{Prob}\left[Y \geq \frac{c}{\sigma} + \sigma\log(b)\right].$$

Now, if $q = 1/2$, then $\log(b) = 0$. Hence the probability of failure is simply:

$$\mathrm{Prob}\left[Y \geq \frac{c}{\sigma}\right] \longrightarrow \frac{1}{2} = q \quad \text{as} \quad \sigma \to \infty.$$

If $q > 1/2$, then $q > 1 - q$ and $\log(b) < 0$. Consequently,

$$\mathrm{Prob}\left[Y \geq \frac{c}{\sigma} - \sigma\log(b)\right] \longrightarrow 0,$$

while

$$\text{Prob}\left[Y \geq \frac{c}{\sigma} + \sigma \log(b)\right] \longrightarrow 1,$$

as $\sigma \to \infty$. Hence,

$$\text{Prob}[\hat{\eta} \neq \eta] \longrightarrow 1 - q \quad \text{as} \quad \sigma \to \infty.$$

That is, the probability of success converges to q. Finally, if $q < 1/2$, then $\log(b) > 0$ and a similar reasoning shows the probability of success converges to $1 - q$. In all cases, the probability of success of the best possible deterministic estimator converges to $\max(q, 1 - q)$.

D. Proof of Proposition 4.2

In the limit,

$$(a_y^1)^2 = \frac{\gamma^2}{L^2} \sum_{i=0}^{L-1} \sum_{j=0}^{L-1} x[i]x[j].$$

Similarly,

$$\sum_{\ell=1}^{L-1} a_y^2[\ell] = \frac{\gamma}{L} \sum_{\ell=1}^{L-1} \sum_{i=0}^{L-1-\ell} x[i]x[i+\ell],$$

and $a_y^2[0] = \frac{\gamma}{L} \sum_{i=0}^{L-1} x^2[i] + \sigma^2$. The proof is concluded by noting that $a_x^2[-\ell] = a_x^2[\ell]$.

E. Proof of Proposition 4.3

We prove that both σ and γ are identifiable from the observed first three moments of y. For convenience, we work with $\beta = \gamma/L$ rather than γ itself. To this end, we construct two quadratic equations satisfied by β and whose coefficients can be computed from observable quantities (in the limit). Then, we show that these equations are independent, and hence that β is uniquely defined. Given β, we can estimate σ using Proposition 4.2.

Throughout the proof, it is important to distinguish between observed and unobserved values. We denote the observed values by E_i or a_y^1, a_y^2, a_y^3. We use F_i to denote functions of the signal's autocorrelations (which are not directly observable).

In the limit $N \to \infty$, almost surely, $a_y^1 = \beta(\mathbf{1}^T x)$ and $a_y^2[0] = \beta\|x\|^2 + \sigma^2$, where $\mathbf{1} \in \mathbb{R}^L$ is the vector of all-ones. (In this whole section, for clarity, we now omit to specify that identities hold almost surely in the limit.) Consider the product:

$$E_1 := a_y^1 a_y^2[0] = (\beta(\mathbf{1}^T x))(\beta\|x\|^2 + \sigma^2)$$
$$= \sigma^2 a_y^1 + L\beta^2 F_1, \qquad [13]$$

where $F_1 := a_x^3[0,0] + \sum_{j=1}^{L-1}(a_x^3[j,j] + a_x^3[0,j])$. The terms of F_1 can also be estimated from a_y^3, while taking the scaling and bias terms into account. This yields another observable:

$$E_2 := a_y^3[0,0] + \sum_{j=1}^{L-1}(a_y^3[j,j] + a_y^3[0,j])$$
$$= L\beta F_1 + (2L+1)\sigma^2 a_y^1. \qquad [14]$$

Therefore, from Eq. (13) and Eq. (14) we get:

$$E_2\beta - (2L+1)\sigma^2\beta a_y^1 = E_1 - \sigma^2 a_y^1. \qquad [15]$$

Let $E_3 := a_y^2[0] + 2\sum_{j=1}^{L-1} a_y^2[j]$; recall from Proposition 4.2:

$$\sigma^2 = E_3 - (a_y^1)^2/\beta. \qquad [16]$$

Plugging into Eq. (15) and rearranging, we get a first quadratic equation in β,

$$\mathcal{A}\beta^2 + \mathcal{B}\beta + \mathcal{C} = 0, \qquad [17]$$

where

$$\mathcal{A} = E_2 - (2L+1)a_y^1 E_3,$$
$$\mathcal{B} = -E_1 + (2L+1)(a_y^1)^3 + a_y^1 E_3,$$
$$\mathcal{C} = -(a_y^1)^3.$$

Importantly, these coefficients are observable quantities. As we assume throughout this proof that x has nonzero mean, $a_y^1 \neq 0$ and we conclude that this equation is non-trivial.

Next, we derive the second quadratic equation for β. We notice that

$$E_4 := \frac{1}{L}(a_y^1)^3 = \frac{1}{L}\beta^3(\mathbf{1}^T x)^3 = \beta^3 F_2, \qquad [18]$$

where $F_2 = \frac{1}{L}(\mathbf{1}^T x)^3$, and we can work out that:

$$F_2 = a_x^3[0,0] + 3\sum_{j=1}^{L-1}\left(a_x^3[j,j] + a_x^3[0,j]\right) + 6\sum_{1 \leq i < j \leq L-1} a_x^3[i,j].$$

Once again, F_2 can be estimated from a_y^3, taking bias and scaling into account:

$$E_5 := a_y^3[0,0] + 3\sum_{j=1}^{L-1}\left(a_y^3[j,j] + a_y^3[0,j]\right) + 6\sum_{1 \leq i < j \leq L-1} a_y^3[i,j]$$
$$= L\beta F_2 + (6L-3)\sigma^2 a_y^1. \qquad [19]$$

Consider the following ratio:

$$\frac{E_5}{E_4} = \frac{L}{\beta^2} + \frac{(6L-3)\sigma^2 a_y^1}{E_4}.$$

From the latter, we deduce:

$$\sigma^2 = \frac{E_5}{a_y^1(6L-3)} - \frac{LE_4}{\beta^2 a_y^1(6L-3)}.$$

Using Eq. (16) and rearranging, we get the second quadratic:

$$\mathcal{D}\beta^2 + \mathcal{E}\beta + \mathcal{F} = 0, \qquad [20]$$

where

$$\mathcal{D} = E_3 - \frac{E_5}{a_y^1(6L-3)},$$
$$\mathcal{E} = -(a_y^1)^2,$$
$$\mathcal{F} = \frac{LE_4}{a_y^1(6L-3)}.$$

It is also non-trivial since $E_4 \neq 0$.

To complete the proof, we need to show that the two quadratic equations Eq. (17) and Eq. (20) are independent. To this end, it is enough to show that the ratios between coefficients differ. From Eq. (17) and Eq. (13), we have:

$$\frac{\mathcal{B}}{\mathcal{C}} = \frac{E_1 - (2L+1)(a_y^1)^3 - a_y^1 E_3}{(a_y^1)^3}$$
$$= \frac{a_y^2[0] - (2L+1)(a_y^1)^2 - E_3}{(a_y^1)^2}.$$

Bendory *et al.*

PNAS | **September 7, 2018** | vol. XXX | no. XX | **11**

In addition, using Eq. (18),

$$\frac{\mathcal{E}}{\mathcal{F}} = \frac{(3-6L)(a_y^1)^3}{LE_4} = 3 - 6L.$$

For contradiction, suppose that the quadratics are dependent. Then, $\frac{\mathcal{B}}{\mathcal{C}} = \frac{\mathcal{E}}{\mathcal{F}}$, that is,

$$a_y^2[0] - (2L+1)(a_y^1)^2 - E_3 = (a_y^1)^2(3-6L).$$

Rewriting the identity in terms of x and dividing by β we get:

$$4(L-1)\beta(\mathbf{1}^\top x)^2 - (\mathbf{1}^\top x)^2 + \|x\|^2 = 0. \qquad [21]$$

For generic x, this polynomial equation is not satisfied so that the quadratic equations are independent. Furthermore, from the inequality $L\|x\|^2 \geq (\mathbf{1}^\top x)^2$ it follows immediately that the equations must be independent so long as

$$\beta > \frac{1}{4L}.$$

F. Autocorrelations for the cryo-EM problem

A. Model and autocorrelation functions. Let ϕ be the Coulomb potential representing the molecule we aim to recover. We assume that molecule is real-valued and smooth. In spherical coordinates, its 3-D Fourier transform $\widehat{\phi}$ admits a finite expansion of the form

$$\widehat{\phi}(ck,\theta,\varphi) = \sum_{\ell=0}^{L} \sum_{m=-\ell}^{\ell} \sum_{s=1}^{S(\ell)} x_{\ell,m,s} Y_\ell^m(\theta,\varphi) j_{\ell,s}(k), \quad k \leq 1,$$

$$[22]$$

where c is the bandlimit, $\{S(\ell)\}$ [to check consistency of S_l] are determined using the Nyquist criterion as described in (40), $j_{\ell,s}$ is the normalized spherical Bessel functions given by [Amit: why 2?]

$$j_{\ell,s}(k) = \frac{4}{|j_{\ell+1}(u_{\ell,s})|} j_\ell(2u_{\ell,s}k),$$

j_ℓ is the spherical Bessel function of order ℓ and $u_{\ell,s}$ is the sth positive zero of j_ℓ. We use the complex spherical harmonics Y_ℓ^m defined by

$$Y_\ell^m(\theta,\varphi) := \sqrt{\frac{2\ell+1}{4\pi} \cdot \frac{(\ell-m)!}{(\ell+m)!}} P_\ell^m(\cos\theta) e^{\iota m\varphi},$$

where P_ℓ^m are the associated Legendre polynomials with the Condon-Shortley phase. Sampling at the Nyquist rate dictates $c = 1/2$ (41). Because ϕ is real-valued, $\widehat{\phi}$ is conjugate-symmetric and thus the expansion coefficients satisfy $x_{\ell,-m,s} = (-1)^{\ell+m}\overline{x_{\ell,m,s}}$. Therefore, we only need to recover coefficients $x_{\ell,m,s}$ with $m \geq 0$.

Let I_ω denote the tomographic projection obtained from viewing direction $\omega \in SO(3)$. By the Fourier projection-slice theorem, its 2-D Fourier transform is given by (42): [Amit: why c is missing here? (it appears in [23])]

$$\widehat{I_\omega}(k,\varphi) = \sum_{\ell,m,m',s} x_{\ell,m,s} D_{m',m}^\ell(\omega) Y_\ell^{m'}\left(\frac{\pi}{2},\varphi\right) j_{\ell,s}(k),$$

where $D_{m',m}^\ell(\omega)$ is a Wigner-D matrix. This implies that the projections are also c-bandlimited.

Let $\mathcal{I} \in \mathbb{R}^{N \times N}$ denote a micrograph. We assume it consists of shifted copies of projections contaminated by additive white Gaussian noise:

$$\mathcal{I} = \sum_{t=1}^{M} I_{\omega_t} * \delta_{\mathbf{s}_t} + \varepsilon, \quad \varepsilon \sim \mathcal{N}(0,\sigma^2 I), \qquad [23]$$

where the viewing directions ω_t are assumed to be drawn from the uniform distribution over SO(3) and $\mathbf{s}_t$ denotes the location of the center of the tth projection in the micrograph. We assume the projection is discretized on a Cartesian grid of size $P \times P$ and we impose a separation condition so that any two projections are separated by at least $2P-1$ pixels between their upper left corners in each direction, similarly to Eq. (2). Note that Eq. (1) can be also written as a sum of δ functions as in Eq. (23).

Define the pth autocorrelation of $\mathcal{I}$ as

$$a_\mathcal{I}^p[\boldsymbol{\ell}_1,\ldots,\boldsymbol{\ell}_{p-1}] := \frac{1}{N^2} \sum_{\mathbf{i}} \mathcal{I}[\boldsymbol{\ell}]\mathcal{I}[\mathbf{i}+\boldsymbol{\ell}_1] \cdots \mathcal{I}[\mathbf{i}+\boldsymbol{\ell}_{p-1}],$$

where the summation is for $\mathbf{i}$ ranging over the N^2 pixels of the micrograph. Let $\mathcal{I}_1,\ldots\mathcal{I}_K$ denote a set of K micrographs. Under the specified conditions, we show in the next section that the first three autocorrelations of the micrographs are related to those of the projections by

$$\lim_{K\to\infty} \frac{1}{K} \sum_{i=1}^{K} a_{\mathcal{I}_i}^p[\boldsymbol{\ell}_1,\ldots,\boldsymbol{\ell}_{p-1}] = \gamma \left\langle a_{I_\omega}^p[\boldsymbol{\ell}_1,\ldots,\boldsymbol{\ell}_{p-1}] \right\rangle_\omega \quad [24]$$

$$+ b_p[\boldsymbol{\ell}_1,\ldots,\boldsymbol{\ell}_{p-1}],$$

$$p = 1,2,3, \quad \boldsymbol{\ell}_1,\ldots,\boldsymbol{\ell}_{p-1} \in [-(P-1),P-1]^2,$$

where $\langle\cdot\rangle_\omega$ denotes averaging over all possible viewing directions ω and b_p is a bias term. Specifically, $b_1 = 0$ and therefore the mean is unbiased. The bias term of the second-order autocorrelation b_2 depends only on σ^2, the variance of the noise. Hence, if the noise level can be accurately estimated from the micrographs, this bias can be removed. Finally, the bias term of the third-order autocorrelation b_3 depends on the mean of the micrograph and σ^2. Therefore, given sufficiently many projections, we can accurately estimate the quantities $\gamma\langle a_{I_\omega}^p\rangle_\omega$ directly from the micrographs. These quantities are functions of the unknown coefficients $x_{l,m,s}$ and we could proceed to invert their relation, as we did in the toy examples.

In practice, we want to leverage one more feature of the 3-D reconstruction problem. Since all in-plane rotations of the micrographs are equally likely observations, it is desirable in Eq. (24) to average over all in-plane rotations as well. This can be done efficiently using Prolate Spheroidal Wave Functions (PSWFs). We use autocorrelations up to and including the third order. Indeed, second-order autocorrelations are not enough, as was observed already in (11) for a simpler problem where the input is not micrographs but rather picked, perfectly centered particles.

B. Autocorrelation derivation. In this section we prove relation Eq. (24). We note that mathematically taking infinitely many micrographs is equivalent to take one infinitely large micrograph with fixed density γ. Hence, we consider the moments of one micrograph $\mathcal{I}$ in the limit $N \to \infty$ and $\gamma = \lim_{N\to\infty} \frac{MP^2}{N^2} \in (0,1)$. The separation condition guarantees that if $\mathbf{i} = (i,j)$ is in the support of some projection, then

$\mathbf{i} + \boldsymbol{\ell}$ for $\boldsymbol{\ell} \in [-(P-1), P-1]^2$ is either in the support of the same projection or outside the support of any projection.

We begin by calculating the relation between the pth autocorrelation of the clean micrograph and the averaged autocorrelation of the projections. Let us denote the clean micrograph by $\widetilde{\mathcal{I}} = \mathcal{I} - \varepsilon$, where $\mathcal{I}$ and ε are given in Eq. (23). Denote by $\mathcal{S}_t$ the support of the tth particle. Then, we have

$$
\begin{aligned}
a_{\widetilde{\mathcal{I}}}^p & [\boldsymbol{\ell}_1, \dots, \boldsymbol{\ell}_{p-1}] \\
&= \frac{1}{N^2} \sum_{\mathbf{i}} \widetilde{\mathcal{I}}[\mathbf{i}] \widetilde{\mathcal{I}}[\mathbf{i} + \boldsymbol{\ell}_1] \cdots \widetilde{\mathcal{I}}[\mathbf{i} + \boldsymbol{\ell}_{p-1}] \\
&= \frac{1}{N^2} \sum_{t=1}^{M} \sum_{\mathbf{i} \in \mathcal{S}_t} \widetilde{\mathcal{I}}[\mathbf{i}] \widetilde{\mathcal{I}}[\mathbf{i} + \boldsymbol{\ell}_1] \cdots \widetilde{\mathcal{I}}[\mathbf{i} + \boldsymbol{\ell}_{p-1}] \\
&= \frac{MP^2}{N^2} \cdot \frac{1}{M} \sum_{t=1}^{M} \frac{1}{P^2} \sum_{i,j=0}^{P-1} I_{\omega_t}[\mathbf{i}] I_{\omega_t}[\mathbf{i} + \boldsymbol{\ell}_1] \cdots I_{\omega_t}[\mathbf{i} + \boldsymbol{\ell}_{p-1}] \\
&= \frac{MP^2}{N^2} \frac{1}{M} \sum_{t=1}^{M} a_{I_{\omega_t}}^p [\boldsymbol{\ell}_1, \dots, \boldsymbol{\ell}_{p-1}] \\
&\rightarrow \gamma \langle a_{I_\omega}^p [\boldsymbol{\ell}_1, \dots, \boldsymbol{\ell}_{p-1}] \rangle_\omega,
\end{aligned} \qquad [25]
$$

where the average is taken over ω with respect to the distribution of viewing directions. Here, we assume it to be uniform.

In the presence of noise, we get additional bias terms denoted by b_p in Eq. (24). The mean ($p = 1$) is unbiased since the noise is assumed to have zero mean. For the second-order autocorrelation ($p = 2$), we have

$$
\begin{aligned}
a_{\mathcal{I}}^2[\boldsymbol{\ell}] &= \frac{1}{N^2} \sum_{\mathbf{i}} \mathcal{I}[\mathbf{i}] \mathcal{I}[\mathbf{i} + \boldsymbol{\ell}] \\
&= \frac{1}{N^2} \sum_{\mathbf{i}} \widetilde{\mathcal{I}}[\mathbf{i}] \widetilde{\mathcal{I}}[\mathbf{i} + \boldsymbol{\ell}] + \frac{1}{N^2} \sum_{\mathbf{i}} \widetilde{\mathcal{I}}[\mathbf{i}] \varepsilon[\mathbf{i} + \boldsymbol{\ell}] \\
&\quad + \frac{1}{N^2} \sum_{\mathbf{i}} \varepsilon[\mathbf{i}] \widetilde{\mathcal{I}}[\mathbf{i} + \boldsymbol{\ell}] + \frac{1}{N^2} \sum_{\mathbf{i}} \varepsilon[\mathbf{i}] \varepsilon[\mathbf{i} + \boldsymbol{\ell}].
\end{aligned}
$$

The first term is given by Eq. (25) for $p = 2$. The cross terms vanish in the limit. The fourth term is zero unless $\boldsymbol{\ell} = 0$, in which case it converges to σ^2. Thus, we conclude

$$
a_{\mathcal{I}}^2[\boldsymbol{\ell}] \rightarrow \gamma \langle a_{I_\omega}^2[\boldsymbol{\ell}] \rangle_\omega + \sigma^2 \delta[\boldsymbol{\ell}], \qquad [26]
$$

where the bias term $b_2[\boldsymbol{\ell}] = \sigma^2 \delta[\boldsymbol{\ell}]$ depends only on the variance of the noise σ^2.

For the third moments, we get 8 terms:

$$
\begin{aligned}
a_{\mathcal{I}}^3 & [\boldsymbol{\ell}_1, \boldsymbol{\ell}_2] \\
&= \underbrace{\frac{1}{N^2} \sum_{\mathbf{i}} \widetilde{\mathcal{I}}[\mathbf{i}] \widetilde{\mathcal{I}}[\mathbf{i} + \boldsymbol{\ell}_1] \widetilde{\mathcal{I}}[\mathbf{i} + \boldsymbol{\ell}_2]}_{(1)} + \underbrace{\frac{1}{N^2} \sum_{\mathbf{i}} \varepsilon[\mathbf{i}] \varepsilon[\mathbf{i} + \boldsymbol{\ell}_1] \varepsilon[\mathbf{i} + \boldsymbol{\ell}_2]}_{(2)} \\
&+ \underbrace{\frac{1}{N^2} \sum_{\mathbf{i}} \widetilde{\mathcal{I}}[\mathbf{i}] \varepsilon[\mathbf{i} + \boldsymbol{\ell}_1] \widetilde{\mathcal{I}}[\mathbf{i} + \boldsymbol{\ell}_2]}_{(3)} + \underbrace{\frac{1}{N^2} \sum_{\mathbf{i}} \widetilde{\mathcal{I}}[\mathbf{i}] \widetilde{\mathcal{I}}[\mathbf{i} + \boldsymbol{\ell}_1] \varepsilon[\mathbf{i} + \boldsymbol{\ell}_2]}_{(4)} \\
&+ \underbrace{\frac{1}{N^2} \sum_{\mathbf{i}} \varepsilon[\mathbf{i}] \widetilde{\mathcal{I}}[\mathbf{i} + \boldsymbol{\ell}_1] \widetilde{\mathcal{I}}[\mathbf{i} + \boldsymbol{\ell}_2]}_{(5)} + \underbrace{\frac{1}{N^2} \sum_{\mathbf{i}} \widetilde{\mathcal{I}}[\mathbf{i}] \varepsilon[\mathbf{i} + \boldsymbol{\ell}_1] \varepsilon[\mathbf{i} + \boldsymbol{\ell}_2]}_{(6)} \\
&+ \underbrace{\frac{1}{N^2} \sum_{\mathbf{i}} \varepsilon[\mathbf{i}] \varepsilon[\mathbf{i} + \boldsymbol{\ell}_1] \widetilde{\mathcal{I}}[\mathbf{i} + \boldsymbol{\ell}_2]}_{(7)} + \underbrace{\frac{1}{N^2} \sum_{\mathbf{i}} \varepsilon[\mathbf{i}] \widetilde{\mathcal{I}}[\mathbf{i} + \boldsymbol{\ell}_1] \varepsilon[\mathbf{i} + \boldsymbol{\ell}_2]}_{(8)}.
\end{aligned}
$$

We address these terms one by one:

- Term (1) is treated by Eq. (25) for $p = 3$;

- Term (2) is the third-order autocorrelation of pure noise which vanishes in the limit;

- Terms (3)-(5) depend linearly on the noise and hence vanish in the limit;

- For term (6), if $\boldsymbol{\ell}_1 \neq \boldsymbol{\ell}_2$ the term vanishes in the limit. If $\boldsymbol{\ell}_1 = \boldsymbol{\ell}_2$ then

$$
\begin{aligned}
\frac{1}{N^2} \sum_{\mathbf{i}} \widetilde{\mathcal{I}}[\mathbf{i}] \varepsilon[\mathbf{i} + \boldsymbol{\ell}]^2 &= \frac{MP^2}{N^2} \cdot \frac{1}{MP^2} \sum_{t=1}^{M} \sum_{\mathbf{i} \in \mathcal{S}_t} I_{\omega_t}[\mathbf{i}] \varepsilon[\mathbf{i} + \boldsymbol{\ell}]^2 \\
&\rightarrow \gamma \sigma^2 \langle a_{I_\omega}^1 \rangle_\omega,
\end{aligned}
$$

where $\langle a_{I_\omega}^1 \rangle_\omega$ is the mean of the volume.

- Terms (7) and (8) contribute δ functions similar to (6).

Thus, we conclude that

$$
\begin{aligned}
a_{\mathcal{I}}^3[\boldsymbol{\ell}_1, \boldsymbol{\ell}_2] &\rightarrow \gamma \langle a_{I_\omega}^3[\boldsymbol{\ell}_1, \boldsymbol{\ell}_2] \rangle_\omega \\
&+ \gamma \sigma^2 \langle a_{I_\omega}^1 \rangle_\omega \Big(\delta[\boldsymbol{\ell}_1 - \boldsymbol{\ell}_2] + \delta[\boldsymbol{\ell}_1] + \delta[\boldsymbol{\ell}_2] \Big), \quad [27]
\end{aligned}
$$

where the second term is the bias $b_3[\boldsymbol{\ell}_1, \boldsymbol{\ell}_2]$. Note that $\gamma \langle a_{I_\omega}^1 \rangle_\omega$ is approximately the mean of the micrograph since $a_{\mathcal{I}}^1 \approx a_{\widetilde{\mathcal{I}}}^1 \approx \gamma \langle a_{I_\omega}^1 \rangle_\omega$. Therefore, we do not need prior knowledge of γ to effectively debias the third-order autocorrelation.

C. Accounting for all in-plane rotations. We represent our autocorrelations using Prolate Spheroidal Wave Functions (PSWFs) $\{\psi_{k,q}\}$ where $k \geq 0, q \geq 1$ are integers (43). As we demonstrate below, this makes it easier to account for the fact that all in-plane rotations of the micrographs are equally likely observations. This is only a concern for the second and third order autocorrelations. Below, we start with $p = 2$. The PSWFs are eigenfunctions of the truncated Fourier transform and are given in polar coordinates by[¶]

$$
\psi_{k,q}(r, \varphi) = \begin{cases} \frac{1}{\sqrt{8\pi}} \alpha_{k,q} R_{k,q}(r) e^{\iota k \varphi}, & r \leq 1, \\ 0, & r > 1, \end{cases} \qquad [28]
$$

[¶] A different normalization is used in (44).

Bendory *et al.*

PNAS | **September 7, 2018** | vol. XXX | no. XX | **13**

where the range of k, q is determined by Eq. (8) in (44), the $R_{k,q}$ are a family of real, one-dimensional functions and the $\alpha_{k,q}$ are scaling factors which will be defined in the next section. The PSWFs are orthogonal on the unit disk.

For $\boldsymbol{\ell} \in [-(P-1), P-1]^2$, let us define

$$\mathfrak{a}^2[k, q] = \sum_{\boldsymbol{\ell}} a_{\mathcal{I}}^2[\boldsymbol{\ell}]\overline{\psi_{k,q}[\boldsymbol{\ell}]}, \qquad [29]$$

where $\psi_{k,q}[\boldsymbol{\ell}] := \psi_{k,q}(\boldsymbol{\ell}/(P-1))$ is a discretization of the PSWFs. Knowledge of these coefficients is essentially equivalent to knowledge of the second-order correlations owing to the following approximate identity:

$$a_{\mathcal{I}}^2[\boldsymbol{\ell}] \approx \sum_{k,q} \mathfrak{a}^2[k, q]\psi_{k,q}[\boldsymbol{\ell}]. \qquad [30]$$

This holds because the continuous PSWFs form an orthogonal basis, and their discretized counterparts are (empirically) almost orthogonal. As a result, for our purposes, the pair of equations above provides a basis expansion for the autocorrelations.

We now proceed to show that the coefficients $\mathfrak{a}^2[k, q]$ can be computed from the micrographs directly. By definition,

$$\mathfrak{a}^2[k, q] = \sum_{\boldsymbol{\ell}} a_{\mathcal{I}}^2[\boldsymbol{\ell}]\overline{\psi_{k,q}[\boldsymbol{\ell}]}$$

$$= \frac{1}{N^2} \sum_{\mathbf{i}} \mathcal{I}[\mathbf{i}] \left(\sum_{\boldsymbol{\ell}} \mathcal{I}[\mathbf{i} + \boldsymbol{\ell}]\overline{\psi_{k,q}[\boldsymbol{\ell}]} \right)$$

$$= \frac{1}{N^2} \sum_{\mathbf{i}} \mathcal{I}[\mathbf{i}] a_{k,q}[\mathbf{i}], \qquad [31]$$

where we defined

$$a_{k,q}[\mathbf{i}] = \sum_{\boldsymbol{\ell}} \mathcal{I}[\mathbf{i} + \boldsymbol{\ell}]\overline{\psi_{k,q}[\boldsymbol{\ell}]}. \qquad [32]$$

These coefficients can be computed efficiently. Indeed, consider a patch of the micrograph $\mathcal{I}$ centered around pixel $\mathbf{i}$ and of size $(2P-1) \times (2P-1)$. This is exactly the patch indexed in the sum above. Hence, using the same approximation as we did in Eq. (30), a direct expansion of that patch in the discretized PSWFs yields the sought coefficients:

$$\mathcal{I}[\mathbf{i} + \boldsymbol{\ell}] \approx \sum_{k,q} a_{k,q}[\mathbf{i}]\psi_{k,q}[\boldsymbol{\ell}]. \qquad [33]$$

Thus, we proceed as follows: for each position $\mathbf{i}$ in the micrograph $\mathcal{I}$, we extract the corresponding patch of size $(2P-1) \times (2P-1)$, expand it in the discretized PSWFs as in Eq. (33), and collect the $a_{k,q}$ as per Eq. (31) to constitute the second-order autocorrelation of the micrograph.

Crucially, following this formalism, it is now straightforward to account for all in-plane rotations and reflections of the micrograph. Indeed, as can be seen from the definition of the (continuous) PSWFs Eq. (28), the effects of rotations and reflections on expansion coefficients of real images are, respectively, phase modulation and conjugation: this is why this the PSWF basis is called *steerable* (44, 45). By analogy in the discrete case, we have the following approximate expansions for a patch rotated about its center $\mathbf{i}$ by an angle α:

$$\mathcal{I}^{\alpha,+}[\mathbf{i} + \boldsymbol{\ell}] \approx \sum_{k,q} a_{k,q} e^{-\iota k\alpha}\psi_{k,q}[\boldsymbol{\ell}],$$

and the reflection followed by a rotation by angle α:

$$\mathcal{I}^{\alpha,-}[\mathbf{i} + \boldsymbol{\ell}] \approx \sum_{k,q} \overline{a_{k,q}}e^{-\iota k\alpha}\psi_{k,q}[\boldsymbol{\ell}].$$

Averaging over all rotations of the patch $\mathcal{I}(\mathbf{i} + \Delta\mathbf{i})$ and its reflection we get

$$\mathfrak{a}^2[k, q] = \frac{1}{N^2} \sum_{\mathbf{i}} \mathcal{I}[\mathbf{i}] \left(\frac{1}{4\pi} \int_0^{2\pi} \left(a_{k,q}[\mathbf{i}] + \overline{a_{k,q}}[\mathbf{i}] \right) e^{-\iota k\alpha} \, d\alpha \right)$$

$$= \delta[k]\frac{1}{N^2} \sum_{\mathbf{i}} \mathcal{I}[\mathbf{i}]a_{0,q}[\mathbf{i}], \qquad [34]$$

where in the last equality we used that $a_{0,q}[\mathbf{i}]$ is real since both $\mathcal{I}$ and $\psi_{0,q}$ are real valued (more generally, $a_{-k,q} = \overline{a_{k,q}}$). Thus, the second-order autocorrelation, though two-dimensional, effectively only provides radial information.

We now follow a similar approach to estimate the bias term b_2. Introduce the coefficients $\mathfrak{b}_2$ as:

$$\mathfrak{b}_2[k, q] = \sigma^2 \sum_{\boldsymbol{\ell}} \delta[\boldsymbol{\ell}]\overline{\psi_{k,q}[\boldsymbol{\ell}]}$$

$$= \sigma^2 \overline{\psi_{k,q}[\mathbf{0}]}$$

$$= \delta[k]\frac{\sigma^2}{\sqrt{2\pi}}R_{0,q}(0),$$

where we used the fact that the functions $R_{k,q}$ are zero at the origin for $k \neq 0$. With this definition, we have the usual approximation:

$$b_2[\boldsymbol{\ell}] = \sigma^2\delta[\boldsymbol{\ell}] \approx \sum_{k,q} \mathfrak{b}_2[k, q]\psi_{k,q}[\boldsymbol{\ell}].$$

We now turn out attention to the third order autocorrelation. Following the same lines, we define the coefficients:

$$\mathfrak{a}^3[k_1, q_1; k_2, q_2] = \sum_{\boldsymbol{\ell}_1, \boldsymbol{\ell}_2} a_{\mathcal{I}}^3[\boldsymbol{\ell}_1, \boldsymbol{\ell}_2]\overline{\psi_{k_1,q_1}[\boldsymbol{\ell}_1]}\psi_{k_2,q_2}[\boldsymbol{\ell}_2]$$

$$= \frac{1}{N^2} \sum_{\mathbf{i}} \mathcal{I}[\mathbf{i}] \left(\sum_{\boldsymbol{\ell}_1} \mathcal{I}[\mathbf{i} + \boldsymbol{\ell}_1]\overline{\psi_{k_1,q_1}[\boldsymbol{\ell}_1]} \right)$$

$$\times \left(\sum_{\boldsymbol{\ell}_2} \mathcal{I}[\mathbf{i} + \boldsymbol{\ell}_2]\psi_{k_2,q_2}[\boldsymbol{\ell}_2] \right)$$

$$= \frac{1}{N^2} \sum_{\mathbf{i}} \mathcal{I}[\mathbf{i}]a_{k_1,q_1}[\mathbf{i}]\overline{a_{k_2,q_2}[\mathbf{i}]},$$

where the patch expansion coefficients $a_{k,q}$ are as defined in Eq. (32). The coefficients $\mathfrak{a}^3[k_1, q_1; k_2, q_2]$ are related to the third-order autocorrelation via the approximate identity:

$$a_{\mathcal{I}}^3[\boldsymbol{\ell}_1, \boldsymbol{\ell}_2] \approx \sum_{\substack{k_1,q_1 \\ k_2,q_2}} \mathfrak{a}^3[k_1, q_1; k_2, q_2]\psi_{k_1,q_1}[\boldsymbol{\ell}_1]\overline{\psi_{k_2,q_2}[\boldsymbol{\ell}_2]}.$$

Averaging over all rotations of $\mathcal{I}$ and its reflection, we obtain

$$\mathfrak{a}^3[k_1, q_1; k_2, q_2] = \frac{1}{N^2} \sum_{\mathbf{i}} \mathcal{I}[\mathbf{i}] \qquad [35]$$

$$\times \left(\frac{1}{4\pi} \int_0^{2\pi} \left(a_{k_1,q_1}[\mathbf{i}]\overline{a_{k_2,q_2}[\mathbf{i}]} + \overline{a_{k_1,q_1}[\mathbf{i}]}a_{k_2,q_2}[\mathbf{i}] \right) e^{-\iota(k_1-k_2)\alpha}d\alpha \right)$$

$$= \delta[k_1 - k_2]\frac{1}{N^2}\sum_{\mathbf{i}}\mathcal{I}[\mathbf{i}]\Re\{a_{k_1,q_1}[\mathbf{i}]\overline{a_{k_2,q_2}[\mathbf{i}]}\}.$$

Thus, similarly to the second-order autocorrelation, averaging over all in-plane rotations reveals that the 4-D third-order autocorrelation truly only carries information along three dimensions.

Finally, we treat the bias terms:

$$\mathfrak{b}_3[k_1,q_1;k_2,q_2] = \gamma\sigma^2\langle a^1_{I_\omega}\rangle_\omega\delta[k_1 - k_2]$$
$$\times\left[\delta[q_1 - q_2] + \delta[k_1]\frac{1}{2\pi}(\alpha_{0,q_1} + \alpha_{0,q_2})R_{0,q_1}(0)R_{0,q_2}(0)\right].$$

Thus,

$$b_3[\boldsymbol{\ell}_1,\boldsymbol{\ell}_2] = \gamma\sigma^2\langle a^1_{I_\omega}\rangle_\omega\Big(\delta[\boldsymbol{\ell}_1 - \boldsymbol{\ell}_2] + \delta[\boldsymbol{\ell}_1] + \delta[\boldsymbol{\ell}_2]\Big)$$
$$\approx\sum_{\substack{k_1,q_1\\k_2,q_2}}\mathfrak{b}_3[k_1,q_1;k_2,q_2]\psi_{k_1,q_1}[\boldsymbol{\ell}_1]\overline{\psi_{k_2,q_2}[\boldsymbol{\ell}_2]}.$$

D. Connection to volume. Until now, we have established simple relations between the autocorrelations of the micrographs and the autocorrelations of the volume. Now, we complete the picture by deriving the connection with the volume itself.

Using the 2-D PSWFs, we can express each projection as

$$\widehat{I}_\omega(ck,\theta) = \sum_{N,n}b_{N,n}(\omega)\psi_{N,n}(k,\theta),$$

where

$$b_{N,n}(\omega) = \frac{4}{\sqrt{2\pi}|\alpha_{N,n}|^2}\int_0^{2\pi}\int_0^1\widehat{I}_\omega(ck,\theta)R_{N,n}(k)e^{-\iota N\theta}k\,dk\,d\theta,$$
$$= \sum_{\ell,m,m',s}x_{\ell,m,s}\left[\frac{\sqrt{8\pi}}{\alpha_{N,n}}Y_\ell^{m'}(\pi/2,0)\right]D_{m',m}^\ell(\omega)$$
$$\times\left(\int_0^1 j_{\ell,s}(k)R_{N,n}(k)k\,dk\right)\left(\frac{1}{2\pi}\int_0^{2\pi}e^{\iota(m'-N)\theta}d\theta\right),$$
$$= \sum_{|N|\leq\ell}\sum_{m,s}x_{\ell,m,s}D_{N,m}^\ell(\omega)\beta_{\ell,s;N,n},$$

where the coefficients

$$\beta_{\ell,s;N,n} := \begin{cases}\frac{\sqrt{8\pi}}{\alpha_{N,n}}Y_\ell^N(\pi/2,0)\int_0^1 j_{\ell,s}(k)R_{N,n}(k)k\,dk, & \ell\geq|N|\\0, & \ell < |N|\end{cases}$$
[36]

can be precomputed. Since the PSWFs are eigenfunctions of the truncated Fourier transform (44) and hence satisfy

$$\alpha_{N,n}\psi_{N,n}(\mathbf{k}) = \int_{||\mathbf{r}||_2\leq 1}\psi_{N,n}(\mathbf{r})e^{\iota c(\mathbf{r}\cdot\mathbf{k})}d\mathbf{r},$$
[37]

we can now express the projection in real space as

$$I_\omega(r,\varphi) = \sum_{N,n}\widehat{\alpha}_{N,n}b_{N,n}(\omega)\psi_{N,n}(r,\varphi)$$
[38]
$$= \sum_{\ell=0}^L\sum_{N,m=-\ell}^\ell\sum_{n=0}^{n_{\max}(N)}\sum_{s=1}^{S(\ell)}x_{\ell,m,s}\widehat{\beta}_{\ell,s;N,n}D_{N,m}^\ell(\omega)\psi_{N,n}(r,\varphi),$$

where $n_{max}(N)$ is chosen according to Eq. (8) in (44), $\alpha_{N,n}$ is the eigenvalue corresponding to the (N,n)th PSWF, $\widehat{\alpha}_{N,n} = (c/2\pi)^2\alpha_{N,n}$, and $\widehat{\beta}_{\ell,s;N,n} = \widehat{\alpha}_{N,n}\beta_{\ell,s;N,n}$.

Third-order autocorrelation. In Eq. (27) and Eq. (35) we have shown how the third-order autocorrelations of the micrographs and the volume are related, and how we can present them in PSWFs. Now, we relate these expressions to the expansion coefficients of the volume itself.

The third-order autocorrelation of the volume can be expressed in terms of Eq. (38):

$$\langle a^3_{I_\omega}[\boldsymbol{\ell}_1,\boldsymbol{\ell}_2]\rangle_\omega = \frac{1}{L^2}\sum_{\mathbf{i}}\langle I_\omega[\mathbf{i}]I_\omega[\mathbf{i}+\boldsymbol{\ell}_1]\overline{I_\omega([\mathbf{i}+\boldsymbol{\ell}_2])}\rangle_\omega,\qquad[39]$$
$$\approx\sum_{\substack{N_1,n_1\\N_2,n_2\\N_3,n_3}}\langle b_{N_1,n_1}(\omega)b_{N_2,n_2}(\omega)\overline{b_{N_3,n_3}}(\omega)\rangle_\omega$$
$$\times\frac{1}{L^2}\sum_{\mathbf{i}}\psi_{N_1,n_1}[\mathbf{i}]\psi_{N_2,n_2}[\mathbf{i}+\boldsymbol{\ell}_1]\overline{\psi_{N_3,n_3}([\mathbf{i}+\boldsymbol{\ell}_2])},$$

where the approximation is due to discretization. Now,

$$\langle b_{N_1,n_1}(\omega)b_{N_2,n_2}(\omega)\overline{b_{N_3,n_3}}(\omega)\rangle_\omega$$
$$= \sum_{\substack{\ell_1,m_1,s_1\\\ell_2,m_2,s_2\\\ell_3,m_3,s_3}}x_{\ell_1,m_1,s_1}x_{\ell_2,m_2,s_2}\overline{x_{\ell_3,m_3,s_3}}$$
$$\times\langle D_{N_1,m_1}^{\ell_1}(\omega)D_{N_2,m_2}^{\ell_2}(\omega)\overline{D_{N_3,m_3}^{\ell_3}}(\omega)\rangle_\omega$$
$$\times\widehat{\beta}_{\ell_1,s_1;N_1,n_1}\widehat{\beta}_{\ell_2,s_2;N_2,n_2}\overline{\widehat{\beta}_{\ell_3,s_3;N_3,n_3}},$$
[18]

where the latter coefficients are given explicitly in Eq. (36). Using standard properties of D-Wigner functions, we obtain

$$\left\langle D_{N_1,m_1}^{\ell_1}(\omega)D_{N_2,m_2}^{\ell_2}\overline{D_{N_3,m_3}^{\ell_3}}\right\rangle_\omega = (-1)^{N_3+m_3}$$
$$\times\begin{pmatrix}\ell_1 & \ell_2 & \ell_3\\N_1 & N_2 & -N_3\end{pmatrix}\begin{pmatrix}\ell_1 & \ell_2 & \ell_3\\m_1 & m_2 & -m_3\end{pmatrix},$$

where $\begin{pmatrix}\ell_1 & \ell_2 & \ell_3\\m_1 & m_2 & m_3\end{pmatrix}$ are called Wigner 3-j symbols. Notably, these terms are zero unless $m_1 + m_2 + m_3 = 0$ and $|\ell_1 - \ell_2| \leq \ell_3 \leq \ell_1 + \ell_2$. Thus, we conclude that

$$\langle b_{N_1,n_1}(\omega)b_{N_2,n_2}(\omega)\overline{b_{N_3,n_3}}(\omega)\rangle_\omega = \delta_{N_3,N_1+N_2}\qquad[40]$$
$$\times\sum_{\substack{\ell_1,m_1,s_1\\\ell_2,m_2,s_2\\s_3}}\sum_{\ell_3=|\ell_1-\ell_2|}^{\min(L,\ell_1+\ell_2)}x_{\ell_1,m_1,s_1}x_{\ell_2,m_2,s_2}\overline{x_{\ell_3,m_1+m2,s_3}}$$
$$\times(-1)^{N_1+N_2+m_1+m_2}\begin{pmatrix}\ell_1 & \ell_2 & \ell_3\\N_1 & N_2 & -N_1-N_2\end{pmatrix}$$
$$\times\begin{pmatrix}\ell_1 & \ell_2 & \ell_3\\m_1 & m_2 & -m_1-m_2\end{pmatrix}$$
$$\times\widehat{\beta}_{\ell_1,s_1;N_1,n_1}\widehat{\beta}_{\ell_2,s_2;N_2,n_2}\overline{\widehat{\beta}_{\ell_3,s_3;N_1+N_2,n_3}}.$$

Combining Eq. (40) with Eq. (39) provides the explicit relation between the third-order autocorrelation and the volume.

Recall that we obtain the autocorrelations of the volume in PSWFs coefficients; see Eq. (35). Hence, to conclude the derivation we expand

$$\langle a^3_{I_\omega}[\boldsymbol{\ell}_1,\boldsymbol{\ell}_2]\rangle_\omega = \sum_{k,q_1,q_2}\mathfrak{a}^3_x[k,q_1,q_2]\psi_{k,q_1}[\boldsymbol{\ell}_1]\overline{\psi_{k,q_2}[\boldsymbol{\ell}_2]},$$

Bendory *et al.*

PNAS | **September 7, 2018** | vol. XXX | no. XX | **15**

where we only include the block-diagonal terms in the expansion; the rest are equal to zero. Let

$$\Psi_{\ell,N,s}[\boldsymbol{\ell}] := \sum_{n=0}^{n_{\max}(N)} \widehat{\beta}_{\ell,s;N,n} \psi_{N,n}[\boldsymbol{\ell}],$$

$$\rho_{\ell,N,s}^{(k,q)} := \int_{\boldsymbol{\ell}} \Psi_{\ell,N,s}([\mathbf{i}+\boldsymbol{\ell}])\overline{\psi_{k,q}(\boldsymbol{\ell})}.$$

Then, the final formula reads

$$\mathfrak{a}_x^3[k,q_1,q_2] = \sum_{\substack{\ell_1,m_1,s_1 \\ \ell_2,m_2,s_2 \\ s_3}} \sum_{\ell_3=|\ell_1-\ell_2|}^{\min(L,\ell_1+\ell_2)} x_{\ell_1,m_1,s_1} x_{\ell_2,m_2,s_2} \overline{x_{\ell_3,m_1+m_2,s_3}}$$

$$\times (-1)^{m_1+m_2} \begin{pmatrix} \ell_1 & \ell_2 & \ell_3 \\ m_1 & m_2 & -m_1-m_2 \end{pmatrix} \tag{41}$$

$$\times \sum_{N_1=-\ell_1}^{\ell_1} \sum_{N_2=-\ell_2}^{\ell_2} (-1)^{N_1+N_2} \begin{pmatrix} \ell_1 & \ell_2 & \ell_3 \\ N_1 & N_2 & -N_1-N2 \end{pmatrix}$$

$$\times \frac{1}{L^2} \sum_{\mathbf{i}} \Psi_{\ell_1,N_1,s_1}[\mathbf{i}] \rho_{\ell_2,N_2,s_2}^{(k,q_1)}[\mathbf{i}] \overline{\rho_{\ell_3,N_1+N_2,s_3}^{(k,q_2)}[\mathbf{i}]}.$$

In practice, the last two lines of the above expression for $\mathfrak{a}_x^3[k,q_1,q_2]$ is precomputed, and both the integration over $\mathbf{i}$ and over $\boldsymbol{\ell}$ is performed on the grid of the images in the dataset, to match the integration performed on the actual images.

Second-order autocorrelation. The second-order autocorrelation is easier to derive directly in Fourier space, to avoid integration of shifted PSWFs against centered ones. The relation between the second-order autocorrelation of the micrographs and the volume is given in Eq. (26) and Eq. (34). The connection with the expansion coefficients of the volume can be derived in Fourier space directly from Kam's original formula (11) by setting $\mathbf{k}_1 = \mathbf{k}_2$ to obtain

$$\left\langle a_{\hat{I}_\omega}^2(k,\theta) \right\rangle_\omega = \frac{1}{4\pi} \sum_{\ell,m} \left| \sum_s x_{\ell,m,s} j_{\ell,s}(k) \right|^2$$

$$= \frac{1}{4\pi} \sum_{\substack{\ell,m \\ s_1,s2}} x_{\ell,m,s_1} \overline{x_{\ell,m,s_2}} j_{\ell,s_1}(k) j_{\ell,s_2}(k),$$

where we used the fact that the normalized spherical Bessel functions $j_{\ell,s}$ are real.

As before, we want to derive the relation with respect to the PSWF coefficients of the autocorrelation. Hence, we expand the above in 2-D PSWFs by

$$\left\langle a_{\hat{I}_\omega}^2(k,\theta) \right\rangle_\omega = \sum_q \mathfrak{a}_x^2(q) \psi_{0,q}(k),$$

and conclude that

$$\mathfrak{a}_x^2[q] = \frac{1}{\sqrt{8\pi}} \sum_{\substack{\ell,m \\ s_1,s_2}} x_{\ell,m,s_1} \overline{x_{\ell,m,s_2}} \int_0^1 j_{\ell,s_1}(k) j_{\ell,s_2}(k) R_{0,q}(k) k\, dk.$$

$$\tag{42}$$

The integral on k is precomputed.

The mean. Since $j_{\ell,s}(0) = 0$ unless $\ell = 0$, and since $Y_{0,0}(\theta,\varphi) = \frac{1}{\sqrt{4\pi}}$, we conclude from Eq. (22) that

$$\mathfrak{a}_x^1 = \langle a_{I_\omega}^1 \rangle_\omega = \widehat{\phi}(\mathbf{0}) = \frac{1}{\sqrt{4\pi}} \sum_s x_{0,0,s} j_{0,s}(0). \tag{43}$$